

Understanding the Tricks of Deep Learning in Medical Image Segmentation: Challenges and Future Directions

Dong Zhang[†], Yi Lin[†], Hao Chen^{*}, Zhuotao Tian, Xin Yang, Jinhui Tang, Kwang-Ting Cheng, *Fellow, IEEE*

Abstract—Over the past few years, the rapid development of deep learning technologies for computer vision has significantly improved the performance of medical image segmentation (MedISeg). However, the diverse implementation strategies of various models have led to an extremely complex MedISeg system, resulting in a potential problem of unfair result comparisons. In this paper, we collect a series of MedISeg tricks for different model implementation phases (*i.e.*, pre-training model, data pre-processing, data augmentation, model implementation, model inference, and result post-processing), and experimentally explore the effectiveness of these tricks on consistent baselines. With the extensive experimental results on both the representative 2D and 3D medical image datasets, we explicitly clarify the effect of these tricks. Moreover, based on the surveyed tricks, we also open-sourced a strong MedISeg repository, where each component has the advantage of plug-and-play. We believe that this milestone work not only completes a comprehensive and complementary survey of the state-of-the-art MedISeg approaches, but also offers a practical guide for addressing the future medical image processing challenges including but not limited to small dataset, class imbalance learning, multi-modality learning, and domain adaptation. The code and training weights have been released at: [MedISeg](#).

Index Terms—Medical Image Analysis, Convolutional Neural Networks, Medical Image Segmentation, Computer Applications.

1 INTRODUCTION

MEDICAL image segmentation (MedISeg) is one of the most representative and comprehensive research topics in both communities of computer vision and medical image analysis [1]–[3]. It can not only recognize the object category but also locate the pixel-level positions [4]–[9]. In clinical practice, MedISeg has been successfully used in a wide range of potential applications with qualitative and quantitative analyses, *e.g.*, cancer diagnosis [10], tumor change detection [11], treatment planning [12], and computer-integrated surgery [13]. To achieve satisfactory performance, one of the challenges is to enable the segmentation model to learn a set of rich yet discriminative features effectively and efficiently [14]–[17].

In recent years, the performance of MedISeg has been greatly improved [5], [19]–[27], thanks to the remarkable progress in deep image processing technologies [17], [18], [28]–[30]. Advanced backbone networks (*e.g.*, AlexNet [31], VGG [32], ResNet [18], DenseNet [30], MobilNet [33], ShuffleNet [34], ResNeXt [35], HRNet [36], RegNet [37], ViT [38], SwinTransformer [39], CMT [40], ConFormer [41], CvT [42])

- D. Zhang, Y. Lin, H. Chen, and K. Cheng are with the Department of Computer Science and Engineering, The Hong Kong University of Science and Technology, Hong Kong, China. E-mail: {dongz, jhc, tim-cheng}@ust.hk; yi.lin@connect.ust.hk.
- Z. Tian is with SmartMore Inc, China. E-mail: zttian@cse.cuhk.edu.hk.
- X. Yang is with the Department of Electronic Information and Communications, Huazhong University of Science and Technology, Wuhan 430074, China. E-mail: xinyang2014@hust.edu.cn.
- J. Tang is with the School of Computer Science and Engineering, Nanjing University of Science and Technology, Nanjing 210094, China. E-mail: jinhuitang@njjust.edu.cn.

[†] These two authors contributed equally to this work.

^{*} Corresponding author: Hao Chen.

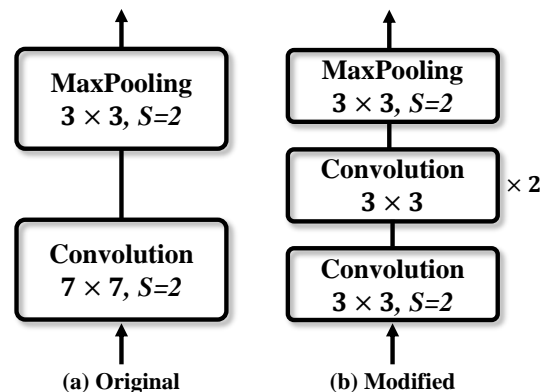


Fig. 1. Two implementation schemes of the input stem in ResNet [18], where (a) is the original implementation as claimed in its paper, and (b) is the modified implementation to reduce the computational costs. “ S ” denotes the stride size. “ $\times 2$ ” denotes that this block is repeated twice.

inherently encode rich semantic feature representations, directly facilitating the MedISeg capacity. At the same time, some certain elaborate feature regulation methods (*e.g.*, lateral connection [43], residual mapping [18], [30], encoder-decoder scheme [44], [45], dense connection [8], [46], feature pyramid [47], [48], and the global context aggregation [49], [50]) can boost the recognition performance. The integration of these sophisticated elements is the main reason that the MedISeg system performs so well. Besides, some training strategies (*e.g.*, co-training [51], [52], co-teaching [53], [54], co-learning [55], [56], and test-time-training [57], [58]) and loss functions (*e.g.*, dice loss and Lovasz-softmax loss [59], [60]) are also indispensable components that can affect the MedISeg performance [61], [62].

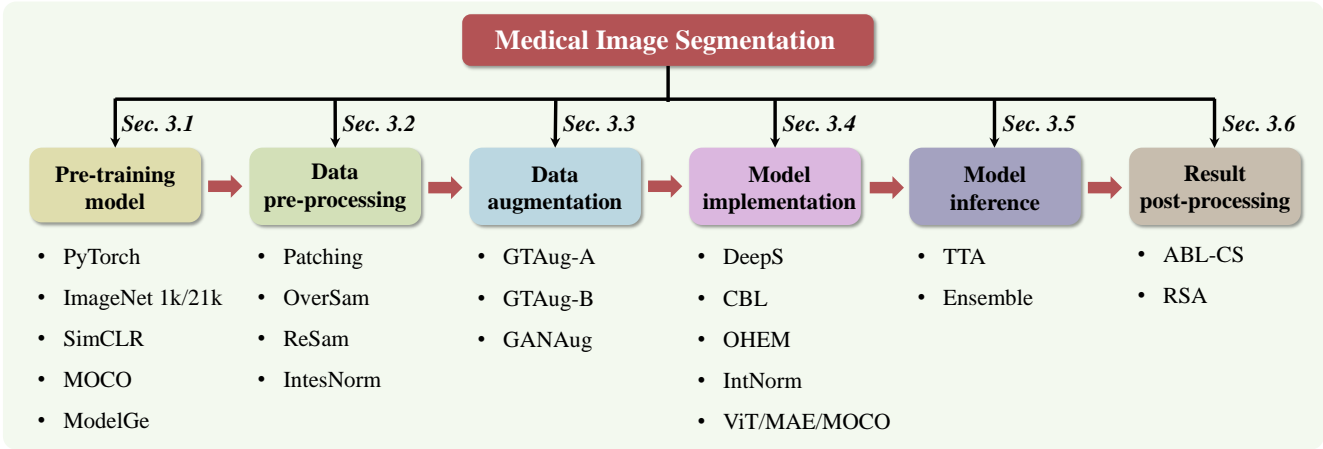


Fig. 2. An illustration of the surveyed tricks and their latent relations. We separate a MedISeg system into six implementation phases, which are pre-training model, data pre-processing, data augmentation, model implementation, model inference, and result post-processing. For each phase of tricks, we experimentally explore their effectiveness on two typical semantic segmentation baselines, namely the 2D-UNet [44] and 3D-UNet [77] with the help of four medical image segmentation datasets, *i.e.*, 2D ISIC 2018 [78], 2D CoNIC [79], 3D KiTS19 [80], and 3D LiTS [67].

However, signs of progress are not proposed solely, they are usually mixed with the existing methods [63], [64], leading to an extremely complex MedISeg system. In particular, at the present moment, an unabridged MedISeg system is usually composed of a large number of implementation details (including some non-learning model-agnostic pre-processing procedures) to achieve the desirable state-of-the-art performance [5], [65]–[70]. Unfortunately, in the current complex MedISeg systems, some marginal implementation strategies (also known as “tricks”) are often disregarded, despite their significant impact on the system’s performance. For example, as illustrated in Figure 1, in the modified input stem of the prevalent ResNet [18] architecture (which is commonly treated as a prevailing backbone network for an MedISeg model), three cumulated 3×3 convolutional layers (in Figure 1 (b)) are used to replace the original 7×7 convolutional layer (in Figure 1 (a)) in the input stem to reduce the computational costs [71]–[73]. Although this subtle change can significantly improve accuracy [30], [64], [74]–[76], few publications explicitly mention this. Therefore, result comparisons of the performance based on such a modified implementation and the performance based on the original implementation are inherently unfair.

The devil is in the details. In this work, to reveal effects of tricks on an MedISeg model, as illustrated in Figure 2, according to a complete set of implementation phases including pre-training model (*ref.* Sec. 3.1), data pre-processing (*ref.* Sec. 3.2), data augmentation (*ref.* Sec. 3.3), model implementation (*ref.* Sec. 3.4), model inference (*ref.* Sec. 3.5), and result post-processing (*ref.* Sec. 3.6), we first collect a series of representative tricks that are easily overlooked in the current MedISeg models. Then, the effectiveness of these tricks is experimentally explored on consistent segmentation baselines including the typical 2D-UNet [44] and 3D-UNet [77] with the help of the representative backbones, such that the influence of model variants (*i.e.*, performance changes due to model changes) can be avoided. Compared to existing paper-driven technical surveys that only blandly focus on the advantage and limitation analyses of the image segmentation model, our work provides a large number of solid experimental results and is more technically operable for future work. Based on extensive experimental results on

four medical image datasets (*i.e.*, the challenging 2D ISIC 2018 lesion boundary segmentation dataset [78], 2D colon nuclei identification and counting challenge dataset [79], [81], 3D kidney tumor segmentation 2019 dataset [80], and 3D liver tumor segmentation challenge dataset [67]), we explicitly clarify the effect of these tricks. Moreover, based on the surveyed tricks and the used baseline models, we also open-sourced a strong MedISeg repository, where each of its component has the advantage of plug-and-play. It is believed that this milestone work not only completes a comprehensive technological survey of the state-of-the-art MedISeg approaches, but also offers a practical guide for addressing future medical image processing (especially the dense image predicted tasks) challenges including small dataset learning, class imbalance learning, multi-modality learning, and domain adaptation.

The main contributions are summarized as follows:

- We collect a series of fundamental MedISeg tricks for different implementation phases, and experimentally explore the effectiveness of these tricks on consistent baseline models.
- We explicitly clarify the effectiveness of these tricks, and a large number of solid experimental results on both 2D and 3D medical image datasets compensate for the implementation neglect in MedISeg.
- We open-sourced a strong MedISeg repository, which includes rich segmentation tricks and each trick has the advantage of plug-and-play.
- This milestone work will facilitate subsequent efforts to compare the experimental results of the MedISeg model under a fair environment.
- This work will provide practical guidance for a wide range of medical image processing especially semantic segmentation challenges in the future.

2 PRELIMINARIES

2.1 Baseline Models

In this work, ensure the comprehensiveness of the experiment, we choose the commonly used and representative 2D-UNet [44] and 3D-UNet [77] as our baseline models. Details of these two baselines are as follows:

2.1.1 2D-UNet

The 2D-UNet is a widely used architecture for medical image segmentation [82]–[86]. It consists of an encoder network and a decoder network. The encoder network follows the fully convolutional architecture and comprises four spatial-tapering stages, each consisting of two 3×3 convolutional layers followed by a rectified linear unit (ReLU) activation function [87], [88] and a global max pooling layer (with stride size $S = 2$). The decoder network, which takes the output of the encoder network as input, also has four stages that correspond to the same spatial encoder stages. Each decoder stage uses a 2D transposed convolutional operator to upsample feature maps $2 \times$ via bilinear interpolation operation [89]. Then, two 3×3 convolutional layers and a ReLU activation function [87], [88] are deployed in sequence. In the final decoder network layer, the channel size of the output feature maps is assigned to the class size of the used dataset via a 2×2 convolutional layer.

2.1.2 3D-UNet

The 3D-UNet shares a similar network architecture with the 2D-UNet [44], consisting of a 3D encoder network and a 3D decoder network [90]–[95]. It is commonly used for 3D image segmentation [96]–[98]. The primary differences between 3D-UNet and 2D-UNet are: i) the 2D convolution layer is replaced with a 3D convolution layer [99]; ii) a lateral connection is added between the same level of the encoder and decoder stages, with the same spatial and channel size; and iii) input image intensity normalization is applied using a normalization layer [100] [87], [88].

2.2 Experimental Datasets

To ensure a comprehensive experimental evaluation and avoid bias towards characteristics of a specific dataset, we selected four representative medical image datasets in this paper. These include a 2D dataset with a common object size, namely the ISIC 2018 Lesion Boundary Segmentation dataset [78]; a 2D dataset with small object size, the Colon Nuclei Identification and Counting Challenge (CoNIC) dataset [79], [81], [101]; the 3D Kidney Tumor Segmentation 2019 (KiTS19) dataset [80]; and the 3D Liver Tumor Segmentation Challenge (LiTS) dataset [67]. Details of each dataset are introduced as follows:

2.2.1 2D ISIC 2018

The ISIC 2018 dataset [78] is a challenging yet representative 2D skin lesion boundary segmentation dataset in the computer-aided diagnosis domain. It consists of 2,594 JPEG dermoscopic images and 2,594 PNG ground truth (GT) images, with one or more lesion regions of varying sizes in each image. Each skin lesion image has a uniform spatial size of 600×450 . We only need to segment two categories of regions in this dataset, namely the foreground “lesion” region and the “background”. For our experiments, we randomly split the dataset into 80% training and 20% test sets, as done in previous studies [102], [103]. In each cross-validation, we further randomly split 10% of the training set as the validation set.

2.2.2 2D CoNIC

The 2D CoNIC challenge dataset comprises images from the Lizard dataset [81], which includes six nuclear categories (*i.e.*, “epithelial cells”, “connective tissue cells”, “lymphocytes”, “plasma cells”, “neutrophils”, and “eosinophils”), and one “background”. Each original image in the Lizard dataset [79], [81], [101] has a ground truth label that contains information about the instance map, nuclear categories, bounding boxes segmentation mask, and nucleus counts. For our experiments, we use the segmentation mask for image segmentation and only distinguish between the foreground object “nuclei” and the “background”, resulting in a binary segmentation task as in [78]. The dataset provides 4,981 image patches in RGB format with a size of 256×256 . Following previous studies [104]–[106], we randomly split all images into 80% for training and 20% for testing. In each cross-validation, we further randomly split 10% of the training set as the validation set.

2.2.3 3D KiTS19

The KiTS19 dataset provides 210 high-quality annotated 3D abdominal computed tomography images of patients, consisting of three categories: “kidney”, “tumor”, and “background”. The positions of the kidney and tumor are relatively fixed in the given images. For our experiments, we follow the commonly used binary segmentation settings [80], [107], [108]: settings-i) the foreground “kidney” and the “background”; settings-ii) the foreground “tumor” and the “background”. Although KiTS19 provides other human structures (*e.g.*, ureters, arteries, and veins), they are not in the range that needs to be segmented and are uniformly considered as the background. Each image and its corresponding ground truth mask in KiTS19 are provided in the NIFTI format, including the number of slices (averaging 216 slices), height (512), and width (512). To ensure ground truth quality, we follow previous studies [80], [109] and remove cases 15, 23, 37, 68, 125, and 133 from the original dataset, leaving 204 cases for training and testing. In each cross-validation, we randomly split off 10% from the training set as the validation set, as done in [80], [107]. Although the dataset’s official website provides an additional 90 test cases, the ground truth masks are not publicly accessible, so we exclude these cases from our experiments.

2.2.4 3D LiTS

Liver cancer is a common tumor, primarily affecting men [67], [110], [111]. To advance the automatic segmentation of lesions, LiTS proposes a benchmark based on contrast-enhanced abdominal computed tomography scans. LiTS contains 130 scans for training and 70 scans for testing, with images initially provided in the PNG format and a spatial size of 256×256 . Each image contains two categories: “background” and “liver”. We treat the tumor area and the liver area equivalently, following [112], [113]. During training, all images are clipped to a spatial size of 200×200 . In each cross-validation, we randomly split off 10% from the training set as the validation set, as done in [111].

2.3 Experimental Settings

Platform. All experiments in our work are conducted using the PyTorch deep learning platform [114] with NVIDIA

GeForce RTX 2080 GPUs. To minimize potential coding errors, we utilize PyTorch’s official functions to perform the necessary operations, including basic operations, loss calculations, and metric calculations.

Backbone. Due to the dataset size and network maturity, we employ the widely recognized ResNet-50 [18] as the default backbone network, which follows the classic implementation of the fully convolutional network architecture [17], [115], [116]. We note that the backbone network’s input stem is implemented using the original cumulative convolution method, as depicted in Figure 1 (a).

Evaluation metrics. We employ the commonly used Recall, Precision, Dice [117], and Intersection over Union (IoU) as our primary metrics [80], [108], [109], [118]. In particular, we perform five-fold cross-validation to evaluate the model performance and report the average result.

2.3.1 Implementation Details of 2D-UNet

Following the previous work in [102], [103], 2D training images in ISIC 2018 [78] and in CoNIC [79], [81], [101] are uniformly resized into the same fixed input size of 200×200 , and are also normalized using the mean value and the standard deviation of the ImageNet dataset [119] as in [60], [85], [120]. The initial learning rate is set to 0.0003. The adaptive moment estimation [121] is used as the optimizer, where the weight decay is set to 0.0005. The whole model is trained with 200 training epochs with a batch size of 32, and the results of the best model on the validation set are used for testing as in [59], [108]. Following [8], [67], we employ the commonly used pixel-level cross-entropy [122] loss as the default loss function.

2.3.2 Implementation Details of 3D-UNet

Following the commonly used experimental setting [67], [80], [109]–[111], [118], [123] for KiTS19 [80] and LiTS [67], Hounsfield units are clipped to $[-79, \dots, 304]$ and the voxel spacing is resampled by the coefficient of $3.22 \times 1.62 \times 1.62 \text{ mm}^3$ as in [59], [107], [108]. We down-sample the computed tomography scans on the cross-section and resample it to adjust the z-axis spacing of all data to 1mm for LiTS [67]. The training voxel size (patch size) is set to $96 \times 96 \times 96$, which is just right to be crammed into an NVIDIA GeForce RTX 2080 GPU. The stochastic gradient descent [124] is used as the optimizer, where the momentum is set to 0.9 and the weight decay is set to 0.0001, respectively. The initial learning rate is set to 0.01, and the batch size is set to 2. The model is trained in an end-to-end fashion with 100 epochs, and the results of the best model on the validation set are used for testing as in [59], [108]. The cross-entropy loss is used as the unique loss function as in [123], [125]. In the inference phase, we perform patch-wise overlap with 50% region overlap (*i.e.*, $48 \times 48 \times 48$).

3 METHODS AND EXPERIMENTS

We divide the complete MedISeg system into six phases, with each phase exploring a set of representative tricks empirically. We note that all experiments are conducted using the preliminary settings described in Section 2.3, without any specific modifications mentioned.

3.1 Pre-Training Model

Pre-training models can provide favorable parameters [39], [126], but the impact of different pre-training models is usually overlooked. For instance, when using the popular ImageNet [119] pre-training model, authors frequently state that their network is pre-trained on the ImageNet, without specifying the particular pre-training implementation. However, pre-training on ImageNet can take at least two basic forms (*i.e.*, 1k and 21k versions), and fair result comparisons require detailed pre-training implementation explanations. To this end, in this subsection, we explore six commonly used and publicly available pre-trained weights on MedISeg. These pre-trained weights can be divided into the following two main categories: fully-supervised (*i.e.*, PyTorch official weights [114] and model-oriented ImageNet-1k/21k weights [119]) and self-supervised (*i.e.*, SimCLR weights [127], MoCo weights [128], and Model Genesis (ModelGe) weights [129]).

3.1.1 PyTorch Official Weights

In the PyTorch repository, there are some backbone pre-trained weights provided by `torchvision.models` [114]. These weights are obtained by training the corresponding backbone network for the single-label image classification task on ImageNet-1k dataset [119], where “1k” denotes that this dataset consists of 1,000 classes of the common scenes.

3.1.2 Model-Oriented ImageNet-1k Weights

Besides PyTorch official weights, the model creator usually releases pre-trained weights on ImageNet [119], [130] as well. For example, the model-oriented ImageNet-1k weights can be obtained by training ResNet-50 [18] for image classification on the ImageNet-1k dataset. We then use the obtained trained weights for downstream vision tasks.

3.1.3 Model-Oriented ImageNet-21k Weights

Compared to ImageNet-1k [119], ImageNet-21k is a more general and comprehensive dataset version, which has about 21,000 object classes in total [131] for image classification. Therefore, the trained weights on ImageNet-21k are also conducive to downstream tasks [38], [39], [132].

3.1.4 SimCLR Weights

SimCLR [127] demonstrates that using a learnable nonlinear transformation between feature representations and the contrastive learning loss can improve feature representations [133], [134]. To this end, SimCLR mainly consists of three steps: 1) the input image is grouped into some image patches; 2) different data augmentation strategies are implemented on image patches for different batches; 3) the model is trained to obtain the similar results for the same image patches with different augmentations, and mutually exclude other results. In our work, we use the SimCLR weights that are trained on ImageNet-1k [119] for classification [18].

3.1.5 MoCo Weights

MoCo [128] is one of the classical self-supervised contrastive learning methods. It aims to address the problem of sampled feature inconsistency in the memory bank [135], [136]. To this end, MoCo uses a queue to store and sample the

TABLE 1

Experimental results on different pre-trained weights. “PyTorch”, “Imag-1k”, “Imag-21k”, “SimCLR”, “MOCO” and “ModelGe” denotes the PyTorch [114] official weights, model-oriented ImageNet 1k [131] weights, model-oriented ImageNet 21k [131] weights, SimCLR [127] weights, MOCO [128] weights and the model genesis [129] weights, respectively. “+” means fine-tuning the baseline model on the corresponding weights.

| Methods | Recall (%) | Percision (%) | Dice (%) | IoU (%) | Recall (%) | Percision (%) | Dice (%) | IoU (%) |
|------------------|-------------------------|------------------------|------------------------|------------------------|--------------------------|------------------------|------------------------|------------------------|
| 2D-UNet [44] | ISIC 2018 [78] | | | | CoNIC [81] | | | |
| | 88.18 | 89.88 | 86.89 | 85.80 | 78.12 | 77.25 | 77.23 | 77.58 |
| + PyTorch [114] | 89.28 ^{+1.10} | 90.08 ^{+0.20} | 88.09 ^{+1.20} | 87.07 ^{+1.27} | 78.08 ^{-0.04} | 79.21 ^{+1.96} | 78.08 ^{+0.85} | 78.38 ^{+0.80} |
| + Imag-1k [131] | 89.19 ^{+1.01} | 90.07 ^{+0.19} | 87.99 ^{+1.10} | 86.93 ^{+1.13} | 79.48 ^{+1.36} | 78.69 ^{+1.44} | 78.70 ^{+1.47} | 78.77 ^{+1.19} |
| + Imag-21k [131] | 90.21 ^{+2.03} | 91.48 ^{+1.60} | 89.38 ^{+2.49} | 88.00 ^{+2.20} | 78.79 ^{+0.67} | 79.66 ^{+2.41} | 78.75 ^{+1.52} | 78.91 ^{+1.33} |
| + SimCLR [127] | 88.09 ^{-0.09} | 89.93 ^{+0.05} | 86.95 ^{+0.06} | 85.90 ^{+0.10} | 77.87 ^{-0.25} | 77.44 ^{+0.19} | 77.17 ^{-0.06} | 77.53 ^{-0.05} |
| + MOCO [128] | 87.99 ^{-0.19} | 90.11 ^{+0.23} | 86.88 ^{-0.01} | 85.84 ^{+0.04} | 77.98 ^{-0.14} | 77.65 ^{+0.40} | 77.35 ^{+0.12} | 77.67 ^{+0.09} |
| 3D-UNet [77] | KiTS19 [80]: settings-i | | | | KiTS19 [80]: settings-ii | | | |
| | 91.01 | 95.20 | 92.50 | 87.35 | 27.35 | 46.71 | 29.63 | 21.51 |
| + ModelGe [129] | 90.70 ^{-0.31} | 95.48 ^{+0.28} | 92.29 ^{-0.21} | 87.18 ^{-0.17} | 28.17 ^{+0.82} | 47.62 ^{+0.91} | 29.95 ^{+0.32} | 21.75 ^{+0.24} |

TABLE 2

Experimental results on 3D LiTS dataset [67]. “ModelGe” denotes the model genesis [129] weight. “+” means fine-tuning the baseline model on the corresponding pre-trained weights.

| Methods | Recall (%) | Percision (%) | Dice (%) | IoU (%) |
|-----------------|------------------------|------------------------|------------------------|------------------------|
| 3D-UNet [77] | 89.33 | 84.03 | 86.11 | 76.44 |
| + ModelGe [129] | 90.54 ^{+1.21} | 84.66 ^{+0.63} | 86.99 ^{+0.88} | 77.67 ^{+1.23} |

negative samples; that is, it stores feature vectors of multiple recent batches used for training. In its implementation, the fixed network remains unchanged and a linear layer with the softmax layer is added to the end of the backbone for classification in an unsupervised training manner. In our work, we use the MoCo weights that are trained on ImageNet-1k [119] for classification on ResNet-50 [18].

3.1.6 ModelGe Weights

ModelGe [129] is an advanced self-supervised model pre-training technology, which usually consists of four transformation operations (*i.e.*, non-linear, local pixel shuffling, out-painting, and in-painting) for single image restoration on computed tomography and magnetic resonance imaging images [137], [138]. In its implementation, the network is trained to learn a general visual representation by restoring the original image patch from the transformed one, where the weight for transformation operations is set to 0.9 for non-linear, 0.5 for local pixel shuffling, 0.8 for out-painting, and 0.2 for in-painting following [139]–[141]. Based on the trained model, the obtained trained weights can be used as the pre-trained weights for downstream models.

3.1.7 Experimental Results

Table 1 shows our experimental results on ISIC 2018 [78], CoNIC [79], and KiTS19 [142], while Table 2 presents our results on LiTS [67]. **Overall, we observe that the fine-tuned model outperforms the baseline model trained from scratch.** This observation validates the effectiveness of pre-trained weights and confirms that different pre-trained weights have varying effects. For instance, compared to the baseline results of 2D-UNet [44] on ISIC 2018, pre-trained weights enhance performance across almost all evaluation metrics. Specifically, fine-tuning using ImageNet-21k [119]

pre-trained weights results in a maximum performance gain of 2.03% Recall, 1.60% Precision, 2.49% Dice, and 2.20% IoU, respectively. These gains demonstrate the powerful representation ability of ImageNet-21k [39], [143]. Moreover, the performance gain of the pre-trained model on Precision is relatively small, with an average gain of only 0.45%. We observe similar experimental conclusions on the CoNIC [79] dataset. Specifically, the performance gains on Recall are relatively small (with an average gain of only 0.41%), whereas the performance gains on Precision are relatively large (with an average gain of 1.08%). Therefore, **in 2D medical image segmentation, pre-training using ImageNet-21k is the best choice.** Although the model’s performance drops on some evaluation metrics, we believe that this is not due to the pre-trained weights. The pre-trained weights are obtained from natural scenes, while our task is about medical images, resulting in a domain gap. This problem can be addressed in the future by using pre-trained weights on medical images.

Comparing the fine-tuned 3D-UNet using the released ModelGe weights to the baseline results on KiTS19 [142] and LiTS [67], we observe that using the ModelGe weights can result in a maximum performance gain of 1.21%, 0.91%, 0.88%, and 1.23% in Recall, Precision, Dice, and IoU, respectively, on setting-ii (*i.e.*, segment the foreground “tumor” and the “background”). However, on setting-i on KiTS19 [142], we observe that three-quarters of the performance has a slight drop, with -0.31% Recall, -0.21% Dice, and -0.17% IoU. We speculate that this may be because the kidney region in KiTS19 [142] is more sensitive to the initialized parameters. These 3D experimental results demonstrate that **if there are no better pre-training weights to choose from, ModelGe weights can still achieve satisfactory results overall.** Moreover, this observation inspires us to consider not only the differences between the network architectures of the fine-tuned models but also the state of the used dataset as critical factors [64], [144].

3.2 Data Pre-Processing

Due to the specific data characteristics of 3D medical images (*e.g.*, modalities and resolutions), pre-processing is necessary to achieve satisfactory segmentation performance [145], [146]. In this work, we investigate the effectiveness of four

TABLE 3

Experimental results on data pre-processing tricks, where the two columns of results are experiments of setting-i and setting-ii (as introduced in section 2.2), respectively. “OverSam”, “ReSam”, “IntesNorm” denotes Oversampling [148], Resampling [149], and Intensity normalization [108], respectively. “/o” denotes that this trick is not implemented under this setting, and “NaN” denotes that the model under this setting is corrupted.

| Methods | Recall (%) | Percision (%) | Dice (%) | IoU (%) | Recall (%) | Percision (%) | Dice (%) | IoU (%) |
|-------------------------------|-------------------------|-------------------------|-------------------------|-------------------------|--------------------------|-------------------------|-------------------------|------------------------|
| | KiTS19 [80]: settings-i | | | | KiTS19 [80]: settings-ii | | | |
| 3D-UNet [77] | 91.01 | 95.20 | 92.50 | 87.35 | 27.35 | 46.71 | 29.63 | 21.51 |
| Patching ₃₂ [108] | NaN | NaN | NaN | NaN | NaN | NaN | NaN | NaN |
| Patching ₆₄ [108] | 37.38 _{-53.63} | 59.51 _{-35.69} | 43.47 _{-49.03} | 29.87 _{-57.48} | 5.91 _{-21.44} | 9.40 _{-37.31} | 5.07 _{-24.56} | 2.89 _{-18.62} |
| Patching ₉₆ [108] | 91.01 _{+0.00} | 95.20 _{+0.00} | 92.50 _{+0.00} | 87.35 _{+0.00} | 27.35 _{+0.00} | 46.71 _{+0.00} | 29.63 _{+0.00} | 21.51 _{+0.00} |
| Patching ₁₂₈ [108] | 89.37 _{-1.64} | 95.24 _{+0.04} | 91.56 _{-0.94} | 85.88 _{-1.47} | 37.81 _{+10.46} | 52.28 _{+5.57} | 38.06 _{+8.43} | 28.81 _{+7.30} |
| Patching ₁₆₀ [108] | 92.85 _{+1.84} | 95.47 _{0.27} | 93.79 _{+1.29} | 89.32 _{+1.97} | 38.42 _{+11.07} | 57.39 _{+10.68} | 39.29 _{+9.66} | 29.71 _{+8.20} |
| Patching ₁₉₂ [108] | 92.77 _{+1.76} | 95.02 _{-0.18} | 93.44 _{+0.94} | 88.82 _{+1.47} | 40.32 _{+12.97} | 57.22 _{+10.51} | 40.36 _{+10.73} | 30.83 _{+9.32} |
| + OverSam [148] | 91.85 _{+0.84} | 95.05 _{-0.15} | 92.93 _{+0.43} | 88.08 _{+0.73} | 35.46 _{+8.11} | 53.69 _{+6.98} | 35.69 _{+6.06} | 26.56 _{+5.05} |
| (/o) ReSam [149] | 0.18 _{-90.83} | 25.49 _{-69.71} | 0.35 _{-92.15} | 0.18 _{-87.17} | NaN | NaN | NaN | NaN |
| (/o) IntesNorm [100] | 90.23 _{-0.78} | 95.33 _{+0.13} | 92.20 _{-0.30} | 86.65 _{-0.70} | 27.15 _{-0.20} | 49.29 _{+2.58} | 29.63 _{+0.00} | 21.73 _{+0.22} |

commonly used image pre-processing techniques in 3D-UNet [77]: patching [147], oversampling (OverSam) [148], resampling (ReSam) [149], and intensity normalization (IntesNorm) [108].

3.2.1 Patching

Some medical images, such as MRI [150] and pathology images [147], can be very large in spatial size and lack sufficient training samples, making it impractical to train a MedISeg model directly on these images [151], [152]. Instead, it is common to resample the entire image into smaller image patches at different spatial scales, with or without overlaps. This approach reduces GPU memory requirements and enables more effective model training. The patch size is one of the most critical factors affecting model performance. In our work, following the experimental settings on 3D-UNet [59], [108], we set the training patch size to $96 \times 96 \times 96$ without overlap and the patch size to $96 \times 96 \times 96$ with a 50% region overlap during the inference phase.

3.2.2 OverSam

OverSam [148] is proposed to address the issue of class imbalance between positive and negative samples in the minority class [153]. Currently, a group of OverSam schemes have been proposed, including random oversampling [148], synthetic minority oversampling (SMOTE) [154], borderline SMOTE [155], and adaptive synthetic sampling [156]. Previous experimental results have shown that OverSam does not affect the model slope but can amplify the model intercept [157], [158]. In our work, we adopt the prevailing OverSam scheme as proposed in [108], where 70% of the selected training samples are from random image locations and 30% of the image patches are guaranteed to contain at least one foreground class. This way, each training sample can simultaneously include one foreground image patch and one random image patch.

3.2.3 ReSam

ReSam [149] is proposed to improve the representational ability of the used dataset. Because the available sample ability is sometimes limited and heterogeneous, a better sub-sample dataset can be obtained via a random/nonrandom

ReSam strategy [159], [160]. In its implementation, ReSam mainly consists of four steps: 1) spacing interpolation; 2) window transform; 3) acquisition of mask effective range, and 4) generation of sub-images. Based on the reorganized sub-sample dataset, a better-performing recognition model can be trained [149], [161]. In our baseline implementation, the commonly used random ReSam strategy has been used. To demonstrate its importance in MedISeg, in this section, we explore the effect of the ReSam strategy by removing it (*i.e.*, /o) in our experiments, *i.e.*, the image pixels are directly interpolated and scaled, such that the actual distances represented by the pixels are the same.

3.2.4 IntesNorm

IntesNorm [162] is a specific normalization strategy for medical images [163], [164]. There are usually two commonly used IntesNorm methods: z-scoring for all modalities and another one for computed tomography images [108]. In our work, we mainly explore the effectiveness of IntesNorm by removing it (*i.e.*, /o) on KiTS19 [80] in our experiments. Following the common implementation [108], [162], a global normalization scheme is adopted in this paper, where 0.5% of the foreground voxels is used for clipping and computing the foreground mean, and 99.5% of the foreground voxels is used for computing the standard deviation.

3.2.5 Experimental Results

Table 3 and Table 4 present our experimental results on KiTS19 [142] and LiTS [67], respectively. We observe that the effect of pre-processing operations on setting-ii is more sensitive than that on setting-i, compared to the baseline model on KiTS19 [142]. Specifically, 1) **larger patching sizes result in better overall model performance**. When the patching size is relatively small (*e.g.*, 32), the segmentation model is corrupted on both KiTS19 [142] and LiTS [67]. When the patching size is set to 192, the model on KiTS19 [142] achieves the best performance on setting-ii. Experimental results on LiTS [67] show that the model performance gain increases gradually with the increase of patching size. Although there is a slight performance drop on setting-i under Patching₁₉₂ compared to the baseline performance,

TABLE 4

Experimental results on 3D LiTS dataset [67] on data pre-processing tricks. “OverSam”, “ReSam”, “IntesNorm” denotes Oversampling [148], Resampling [149], and Intensity normalization [108], respectively. “/o” denotes that this trick is not implemented under this setting, and “NaN” denotes that the model under this setting is corrupted.

| Methods | Recall (%) | Precision (%) | Dice (%) | IoU (%) |
|-------------------------------|-------------------------|-------------------------|-------------------------|-------------------------|
| 3D-UNet [77] | 89.33 | 84.03 | 86.11 | 76.44 |
| Patching ₃₂ [108] | NaN | NaN | NaN | NaN |
| Patching ₆₄ [108] | 73.27 _{-16.06} | 78.57 _{-5.46} | 75.14 _{-10.97} | 60.71 _{-15.73} |
| Patching ₉₆ [108] | 89.33 _{+0.00} | 84.03 _{+0.00} | 86.11 _{+0.00} | 76.44 _{+0.00} |
| Patching ₁₂₈ [108] | 92.05 _{+2.72} | 91.55 _{+7.52} | 91.44 _{+5.33} | 84.60 _{+8.16} |
| Patching ₁₆₀ [108] | 93.29 _{+3.96} | 94.94 _{+10.91} | 93.88 _{+7.77} | 88.76 _{+12.32} |
| Patching ₁₉₂ [108] | 93.31 _{+3.98} | 95.35 _{+11.32} | 94.08 _{+7.97} | 89.18 _{+12.74} |
| + OverSam [148] | 89.78 _{+0.45} | 87.55 _{+3.52} | 88.14 _{+2.03} | 79.85 _{+3.41} |
| (/o) ReSam [149] | 73.19 _{-16.14} | 78.86 _{-5.17} | 73.87 _{-12.24} | 60.84 _{-15.60} |
| (/o) IntesNorm [100] | 87.64 _{-1.69} | 81.14 _{-2.89} | 83.68 _{-2.43} | 72.37 _{-4.07} |

this arises from the experimental setting on the image scale rather than the patching scheme [108]. This experimental phenomenon is consistent with the conclusions of previous papers in [59], [108], which recommends using as large an image patch size as GPU memory can accommodate. 2) **OverSam [153], [156] improves model performance overall.** In particular, + OverSam on KiTS19 [142] brings a remarkable performance gain of 0.84% Recall, 0.43% Dice, and 0.73% IoU on setting-i and 9.11% Recall, 6.98% Precision, 6.06% Dice, and 5.05% IoU on setting-ii. 3) **Without ReSam [165], model performance significantly reduces on both KiTS19 [142] and LiTS [67].** For example, on KiTS19, the model can result in a performance decrease of 90.83% Recall, 69.71% Precision, 92.15% Dice, and 87.17% IoU on setting-i. Surprisingly, the model is completely corrupted without using ReSam under setting-ii. 4) **IntesNorm [162] has a relatively weak effect on results on both setting-i and setting-ii on KiTS19.** For example, without using IntesNorm, the baseline 3D-UNet [77] only reduces the max model performance of 0.78% Recall, 0.30% Dice, and 0.70% IoU on setting-i and 0.20% Recall and 0.00% Dice on setting-ii, respectively. However, IntesNorm has a significant effect on experimental results on LiTS [67]. This phenomenon shows that the same method has different effects on different datasets regarding data pre-processing strategies. The experimental results from 2) to 4) validate the importance of OverSam, ReSam, and IntesNorm in MedISeg.

3.3 Data Augmentation

Data augmentation is used to address problems of insufficient training samples and overfitting [166]–[170]. In particular, for medical images, data augmentation is frequently employed [171], [172]. The data augmentation schemes used in MedISeg can be broadly classified into two categories: geometric transformation-based data augmentation (GTAug) [167] and generative adversarial network (GAN)-based data augmentation (GANAug) [169].

3.3.1 GTAug

To eliminate the impact of geometric object variations in training images, such as positions, scales, and viewing

angles, we employ GTAug [167]. GTAug is a widely used data augmentation method that includes flipping, cropping, rotations, translating, color jittering, contrast, simulation of low resolution, Gaussian noise injection, mixing images, random erasing, Gaussian blur, mixup, and cutmix [59], [166], [168], [170]. In our work, we select several commonly used data augmentation methods, including random brightness contrast (with brightness limit = 0.2, contrast limit = 0.2, and $p = 0.5$), random gamma (with gamma limit = (80, 120), and $p = 0.5$), CLAHE, random noise with $p = 0.5$, gamma adjust with $p = 0.5$, shift scale rotate (with shift limit=0.1, scale limit=0.1, rotate limit=45, and $p = 0.5$), horizontal flip with $p = 0.5$, vertical flip with $p = 0.5$, random scale([0.85, 1.25]) with $p = 0.5$, random rotation([90, 180, 279]), and random mirroring along the X, Y, Z axial directions in a MedISeg model.

We divide the above data augmentation schemes into two groups and implement two types of data augmentation, named GTAug-A (*i.e.*, pixel-level transform) and GTAug-B (*i.e.*, spatial-level transform). Specifically, for experiments on 2D-UNet [44], we use random brightness contrast, random gamma, and CLAHE in GTAug-A, and shift scale rotate, horizontal flip, and vertical flip in GTAug-B. All schemes are deployed with their default parameters. For experiments on 3D-UNet [77], we use random noise and gamma adjust in GTAug-A, and random scale, random rotation, and random mirroring in GTAug-B, all with their default parameters.

3.3.2 GANAug

The intrinsic prerequisite for data augmentation is to introduce the domain knowledge or other incremental information into the training dataset [174]–[176]. From this aspect, GANAug can be viewed as a loss function that focuses on guiding the network to generate some real data that is close to the source dataset domain [120], [166]. Especially, given the small dataset, the data distribution fitted by the generative model of GAN is better than that of the discriminative model. Therefore, GANAug is suitable for MedISeg task [177], [178]. In our work, the classical pixel-level image-to-image translation with conditional adversarial networks [173] is used with its default setting.

3.3.3 Experimental Results

In Tables 5 and 6, we present the experimental results of different data augmentation schemes. We observe that, in comparison with the baseline 2D-UNet [44] on ISIC 2018 [78] in Table 5, GTAug-B significantly improves the recognition performance according to all evaluation metrics, while GTAug-A slightly reduces the performance under three metrics, namely -0.51% Recall, -0.02% Dice, and -0.12% IoU. These observations confirm that **the spatial-level transform outperforms the pixel-level transform on 2D images.** In contrast to GTAug, GANAug achieves lower performance, with -0.40% Recall, -0.29% Precision, -0.42% Dice, and -0.16% IoU reductions. The overall performance of GANAug is worse than that of GTAug. When both GTAug and GANAug are applied to 2D-UNet [44] on ISIC 2018 [78] (+ All in Table 5), the model’s performance improves according to three evaluation metrics, namely 0.37% Precision, 0.41% Dice, and 0.83% IoU, resulting in a final performance of 87.77% Recall, 90.25% Precision,

TABLE 5

Experimental results on data augmentation schemes. "GTAug" and "GANAug" denote the geometric transformation-based and the GAN-based data augmentation [173], respectively. "All" denotes that both GTAug and GANAug are used in the model training phase.

| Methods | Recall (%) | Percision (%) | Dice (%) | IoU (%) | Recall (%) | Percision (%) | Dice (%) | IoU (%) |
|----------------|-------------------------|------------------------|------------------------|------------------------|--------------------------|-------------------------|-------------------------|-------------------------|
| 2D-UNet [44] | ISIC 2018 [78] | | | | CoNIC [81] | | | |
| | 88.18 | 89.88 | 86.89 | 85.80 | 78.12 | 77.25 | 77.23 | 77.58 |
| + GTAug-A | 87.67 _{-0.51} | 90.19 _{+0.31} | 86.87 _{-0.02} | 85.68 _{-0.12} | 78.94 _{+0.82} | 77.54 _{+0.29} | 77.87 _{+0.64} | 78.05 _{+0.47} |
| + GTAug-B | 88.32 _{+0.14} | 91.11 _{+1.23} | 88.07 _{+1.18} | 86.98 _{+1.18} | 79.28 _{+1.16} | 82.53 _{+5.28} | 80.33 _{+3.10} | 80.35 _{+2.77} |
| + GANAug [173] | 87.78 _{-0.40} | 89.59 _{-0.29} | 86.47 _{-0.42} | 85.64 _{-0.16} | 78.43 _{+0.31} | 77.05 _{-0.20} | 77.37 _{+0.14} | 77.62 _{+0.04} |
| + All | 87.77 _{-0.41} | 90.25 _{+0.37} | 87.30 _{+0.41} | 86.63 _{+0.83} | 81.17 _{+3.05} | 80.27 _{+3.02} | 80.39 _{+3.16} | 80.13 _{+2.55} |
| 3D-UNet [77] | KiTS19 [80]: settings-i | | | | KiTS19 [80]: settings-ii | | | |
| | 91.01 | 95.20 | 92.50 | 87.35 | 27.35 | 46.71 | 29.63 | 21.51 |
| + GTAug-A | 89.60 _{-1.41} | 95.44 _{+0.24} | 91.65 _{-0.85} | 86.13 _{-1.22} | 21.81 _{-5.54} | 45.89 _{-0.82} | 25.68 _{-3.95} | 18.19 _{-3.32} |
| + GTAug-B | 84.40 _{-6.61} | 94.58 _{-0.62} | 88.00 _{-4.50} | 80.94 _{-6.41} | 14.02 _{-13.33} | 37.70 _{-9.01} | 15.64 _{-13.99} | 10.71 _{-10.80} |
| + GANAug [173] | 91.89 _{+0.88} | 94.88 _{-0.32} | 92.87 _{+0.37} | 87.98 _{+0.63} | 29.19 _{+1.84} | 47.69 _{+0.98} | 30.99 _{+1.36} | 22.89 _{+1.38} |
| + All | 85.97 _{-5.04} | 90.55 _{-4.65} | 86.93 _{-5.57} | 78.91 _{-8.44} | 6.86 _{-20.49} | 30.39 _{-16.32} | 9.93 _{-19.70} | 6.29 _{-15.22} |

TABLE 6

Experimental results on 3D LiTS dataset [67] on different data augmentation schemes. "GTAug" and "GANAug" denote the geometric transformation-based and the generative adversarial network-based data augmentation [173], respectively. "All" denotes that both GTAug and GANAug are used in the model training phase.

| Methods | Recall (%) | Percision (%) | Dice (%) | IoU (%) |
|----------------|-------------------------|------------------------|-------------------------|-------------------------|
| 3D-UNet [77] | 89.33 | 84.03 | 86.11 | 76.44 |
| + GTAug-A | 90.28 _{+0.95} | 84.24 _{+0.21} | 86.62 _{+0.51} | 76.89 _{+0.45} |
| + GTAug-B | 84.85 _{-4.48} | 81.60 _{-2.43} | 82.45 _{-3.66} | 70.97 _{-5.47} |
| + GANAug [173] | 75.83 _{-13.50} | 76.42 _{-7.61} | 75.00 _{-11.11} | 61.49 _{-14.95} |
| + All | 70.32 _{-19.01} | 77.04 _{-6.99} | 71.69 _{-14.42} | 57.89 _{-18.55} |

87.30% Dice, and 86.63% IoU. Comparing the results on the baseline 2D-UNet [44] on CoNIC [79] and ISIC 2018 [78], we observe that almost all values under the evaluation metrics are improved. The comparison of the experimental results on ISIC 2018 [78] and CoNIC [79] shows that GTAug-B can achieve better results on both datasets than GTAug-A and GANAug, highlighting the importance of shift scale rotate, horizontal flip, and vertical flip. Furthermore, the above two sets of experimental results indicate that **we should choose the appropriate data augmentation methods when faced with different datasets**, as discussed in Section 3.1.

Regarding the experimental results on 3D KiTS19 [142] and LiTS [67], we find that, in general, **GANAug can boost the maximum performance gain, while GTAug is barely beneficial on KiTS19 [142]**. In contrast, the experimental results on LiTS [67] show that only GTAug-A is beneficial, while GTAug-B and GANAug are detrimental to the performance. For instance, using GTAug on 3D-UNet on KiTS19 [142] reduces the maximum performance by -13.33% , 9.01% , 13.99% , and 10.80% for Recall, Precision, Dice, and IoU, respectively. In comparison, GANAug achieves performance gains of 0.88% Recall, 0.37% Dice, and 0.63% IoU in setting-i and 1.84% Recall, 0.98% Precision, 1.36% Dice, and 1.38% IoU in setting-ii. When both GTAug and GANAug are applied to KiTS19 [142], the model's performance is even lower, with 85.97% Recall,

90.55% Precision, 86.93% Dice, and 78.91% IoU in setting-i and 6.86% Recall, 30.39% Precision, 9.93% Dice, and 6.29% IoU in setting-ii. In particular, the results in setting-ii show the maximum performance reduction of -20.49% , -16.32% , -19.70% , and -15.22% for Recall, Precision, Dice, and IoU, respectively. The experimental results on LiTS [67] in Table 6 show that GTAug-A can improve every evaluation metric by 0.95% Recall, 0.21% Precision, 0.51% Dice, and 0.45% IoU. In contrast, implementing both GANAug and GTAug at the same time (*i.e.*, +All) leads to the most performance degradation. **These experimental results on KiTS19 [142] and LiTS [67] demonstrate the importance of selecting the appropriate data augmentation methods based on the specific dataset conditions.**

3.4 Model Implementation

MedISeg models typically consist of many implementation details, which is particularly true in current research. In our work, we investigate the effectiveness of three commonly used implementation techniques categorized as: deep supervision (DeepS) [179]; class balance loss (CBL) [180], which includes four loss functions (*i.e.*, CBL_{Dice} [181], CBL_{Focal} [182], CBL_{Tvers} [60], and CBL_{WCE} [183]); online hard example mining (OHEM) [184]; and instance normalization (IntNorm) [100]. Besides, as Transformer-based methods have gained increasing attention for MedISeg in recent years, we also present experimental results on ViT [38], MAE [185], and MoCo [186] for comparison in this section.

3.4.1 DeepS

DeepS [179] is an auxiliary learning technique that was initially proposed in DSN [179] and subsequently used for image classification [187]. This technique is aimed at supervising the backbone network by adding an auxiliary classifier or segmenter on some intermediate hidden layers in a direct or indirect manner [47], [188]–[190]. It can be used to address issues related to training gradient disappearance or slow convergence speed. For image segmentation, this technique is usually implemented by adding an image-level classification loss. In our work, we follow [188], [189], [191]

TABLE 7

Experimental results on some model implementation tricks. “DeepS”, “CBL”, “OHEM”, and IntNorm denotes deep supervision [179], class balance loss [180], online hard example mining [184], and instance normalization [100], respectively.

| Methods | Recall (%) | Precision (%) | Dice (%) | IoU (%) | Recall (%) | Precision (%) | Dice (%) | IoU (%) |
|------------------------------|-------------------------|------------------------|-------------------------|-------------------------|--------------------------|-------------------------|-------------------------|------------------------|
| 2D-UNet [44] | ISIC 2018 [78] | | | | CoNIC [81] | | | |
| | 88.18 | 89.88 | 86.89 | 85.80 | 78.12 | 77.25 | 77.23 | 77.58 |
| + DeepS [179] | 88.91 ^{+0.73} | 89.85 ^{-0.03} | 87.42 ^{+0.53} | 86.18 ^{+0.38} | 78.16 ^{+0.04} | 77.02 ^{-0.23} | 77.13 ^{-0.10} | 77.46 ^{-0.12} |
| + CBL _{Dice} [181] | 89.59 ^{+1.41} | 89.89 ^{+0.01} | 87.71 ^{+0.82} | 86.36 ^{+0.56} | 79.38 ^{+1.26} | 78.37 ^{+1.12} | 78.36 ^{+1.13} | 78.51 ^{+0.93} |
| + CBL _{Focal} [182] | 88.06 ^{-0.12} | 87.32 ^{-2.56} | 85.41 ^{-1.48} | 84.65 ^{-1.15} | 81.78 ^{+3.66} | 73.75 ^{-3.50} | 77.12 ^{-0.11} | 77.24 ^{-0.34} |
| + CBL _{Tvers} [60] | 89.40 ^{+1.22} | 90.19 ^{+0.31} | 87.87 ^{+0.98} | 86.42 ^{+0.62} | 78.65 ^{+0.53} | 78.79 ^{+1.54} | 78.23 ^{+1.00} | 78.40 ^{+0.82} |
| + CBL _{WCE} [183] | 89.72 ^{+1.54} | 88.15 ^{-1.73} | 86.72 ^{-0.17} | 85.63 ^{-0.17} | 82.24 ^{+4.12} | 74.08 ^{-3.17} | 77.54 ^{+0.31} | 77.58 ^{+0.00} |
| + OHEM [184] | 88.06 ^{-0.12} | 89.81 ^{-0.07} | 86.85 ^{-0.04} | 85.80 ^{+0.00} | 77.35 ^{-0.77} | 77.72 ^{+0.47} | 77.06 ^{-0.17} | 77.47 ^{-0.11} |
| 3D-UNet [77] | KiTS19 [80]: settings-i | | | | KiTS19 [80]: settings-ii | | | |
| | 91.01 | 95.20 | 92.50 | 87.35 | 27.35 | 46.71 | 29.63 | 21.51 |
| + DeepS [179] | 90.13 ^{-0.88} | 95.07 ^{-0.13} | 91.88 ^{-0.62} | 86.42 ^{-0.93} | 26.69 ^{-0.66} | 46.03 ^{-0.68} | 29.27 ^{-0.36} | 21.73 ^{+0.22} |
| + CBL _{Dice} [181] | 90.50 ^{-0.51} | 93.24 ^{-1.96} | 91.17 ^{-1.33} | 85.07 ^{-2.28} | 41.91 ^{+14.56} | 44.70 ^{-2.01} | 37.15 ^{+7.52} | 26.74 ^{+5.23} |
| + CBL _{Focal} [182] | 74.88 ^{-16.13} | 95.64 ^{+0.44} | 81.29 ^{-11.21} | 72.27 ^{-15.08} | 9.72 ^{-17.63} | 37.80 ^{-8.91} | 12.98 ^{-16.65} | 8.29 ^{-13.22} |
| + CBL _{Tvers} [60] | 87.72 ^{-3.29} | 93.94 ^{-1.26} | 89.99 ^{-2.51} | 83.13 ^{-4.22} | 35.89 ^{+8.54} | 44.15 ^{-2.56} | 33.49 ^{+3.86} | 23.68 ^{+2.17} |
| + CBL _{WCE} [183] | 92.57 ^{+1.56} | 88.01 ^{-7.19} | 89.49 ^{-3.01} | 82.49 ^{-4.86} | 36.07 ^{+8.72} | 33.53 ^{-13.18} | 29.85 ^{+0.22} | 21.39 ^{-0.12} |
| + OHEM [184] | 91.01 ^{+0.00} | 94.81 ^{-0.39} | 92.17 ^{-0.33} | 86.94 ^{-0.41} | 28.45 ^{+1.10} | 46.68 ^{-0.03} | 30.58 ^{+0.95} | 22.21 ^{+0.70} |
| + IntNorm [100] | 73.53 ^{-17.48} | 85.64 ^{-9.56} | 77.45 ^{-15.05} | 65.93 ^{-21.42} | 16.92 ^{-10.43} | 32.84 ^{-13.87} | 18.45 ^{-11.18} | 11.67 ^{-9.84} |

TABLE 8

Experimental results on 3D LiTS dataset [67] on some model implementation tricks. “DeepS”, “CBL”, “OHEM”, and IntNorm denotes deep supervision [179], class balance loss [180], online hard example mining [184], and instance normalization [100], respectively.

| Methods | Recall (%) | Precision (%) | Dice (%) | IoU (%) |
|------------------------------|-------------------------|-------------------------|-------------------------|-------------------------|
| 3D-UNet [77] | 89.33 | 84.03 | 86.11 | 76.44 |
| + DeepS [179] | 90.42 ^{+1.09} | 84.02 ^{-0.01} | 86.60 ^{+0.49} | 77.17 ^{+0.73} |
| + CBL _{Dice} [181] | 83.09 ^{-6.24} | 71.34 ^{-12.69} | 75.51 ^{-10.60} | 62.45 ^{-13.99} |
| + CBL _{Focal} [182] | 88.37 ^{-0.96} | 81.61 ^{-2.42} | 84.16 ^{-1.95} | 73.16 ^{-3.28} |
| + CBL _{Tvers} [60] | 86.60 ^{-2.73} | 72.93 ^{-11.10} | 78.70 ^{-7.41} | 65.52 ^{-10.92} |
| + CBL _{WCE} [183] | 91.18 ^{+1.85} | 80.27 ^{-3.76} | 84.92 ^{-1.19} | 74.57 ^{-1.87} |
| + OHEM [184] | 90.14 ^{+0.81} | 85.64 ^{+1.61} | 87.35 ^{+1.24} | 78.24 ^{+1.80} |
| + IntNorm [100] | 77.23 ^{-12.10} | 87.27 ^{+3.24} | 80.94 ^{-5.17} | 68.62 ^{-7.82} |

and extract feature maps from the last three decoder layers. We then use a 1×1 convolutional layer to project the lesion mask into the same channel size. Output feature maps from different layers are upsampled into the same spatial size as the input image for the segmentation head network [115], [190], [192] by bilinear interpolations.

3.4.2 CBL

CBL [180] is usually used to learn a general class weight, *i.e.*, the weight for each class is only related to the object category. Compared to some traditional segmentation loss functions (*e.g.*, cross-entropy loss) on the class imbalanced dataset [179], [180], CBL can improve model representational ability. In the used dataset, CBL introduces the effective number of samples to represent the expected volume representations of the selected dataset, and weights different classes by the number of effective samples rather than the number of original samples. In this paper, we

mainly explore the effect of four commonly used CBL loss functions for the class imbalanced problem in medical image domain, including Dice loss (CBL_{Dice}) [181], Focal loss (CBL_{Focal}) [182], Tversky loss (CBL_{Tvers} [60]), and the weighted cross-entropy loss (CBL_{WCE} [183]).

3.4.3 OHEM

The core idea of OHEM [184] is first to filter out some hard learning samples (*i.e.*, images, objects, and pixels) via the loss function, and these selected hard examples all have a high impact on the recognition tasks [184]. Then, these samples are applied to gradient descent in the model training process. Extensive experimental results on different vision tasks show that OHEM is not only efficient but also performs well on various datasets [71], [72], [193], [194]. In our work, we validate the effectiveness of OHEM on both the 2D and 3D medical datasets with its default setting.

3.4.4 IntNorm

IntNorm [100] is a popular normalization algorithm that is suitable for recognition tasks with higher requirements on a single pixel. In its implementation, every single sample and all elements for a single channel of the sample are taken into consideration when computing the statistic normalization [100], [195], [196]. In the medical image domain, an important reason why IntNorm is used is that the batch size is usually set to a small value (especially for 3D images) during the training process, which makes the use of batch normalization invalid. In this paper, we demonstrate the effect of the IntNorm by replacing it with the intensity normalization [108] in 3D experiments.

3.4.5 Transformer-Based Methods.

We take ViT [38], MAE [185], and MoCo [186] in our experiments. ViT divides the input image into multiple

TABLE 9

Experimental results on Transformer-based methods, where “/16” and “/32” are the number of heads in the multi-head attention mechanism.

| Methods | Recall (%) | Precision (%) | Dice (%) | IoU (%) | Recall (%) | Precision (%) | Dice (%) | IoU (%) |
|------------------------|------------------------|------------------------|------------------------|------------------------|-------------------------|-------------------------|-------------------------|-------------------------|
| 2D-UNet [44] | ISIC 2018 [78] | | | | CoNIC [81] | | | |
| | 88.18 | 89.88 | 86.89 | 85.80 | 78.12 | 77.25 | 77.23 | 77.58 |
| ViT-B/16 [38] | 87.56 _{-0.62} | 87.84 _{-2.04} | 85.22 _{-1.67} | 84.45 _{-1.35} | 51.83 _{-26.29} | 63.27 _{-13.98} | 55.57 _{-21.66} | 67.10 _{-10.48} |
| ViT-B/16-MAE [185] | 87.28 _{-0.90} | 87.62 _{-2.26} | 84.83 _{-2.06} | 84.21 _{-1.59} | 51.62 _{-26.50} | 62.98 _{-14.27} | 55.24 _{-21.99} | 66.45 _{-11.13} |
| ViT-B/16-MoCo v3 [186] | 87.93 _{-0.25} | 87.67 _{-2.21} | 85.34 _{-1.55} | 84.58 _{-1.22} | 52.13 _{-25.99} | 63.35 _{-13.90} | 55.78 _{-21.45} | 67.22 _{-10.36} |
| ViT-L/16 [38] | 87.66 _{-0.52} | 87.53 _{-2.35} | 85.04 _{-1.85} | 84.31 _{-1.49} | 51.89 _{-26.23} | 63.10 _{-14.15} | 55.71 _{-21.52} | 67.01 _{-10.57} |
| ViT-B/32 [38] | 83.61 _{-4.57} | 83.17 _{-6.71} | 80.99 _{-5.90} | 81.51 _{-4.29} | 48.96 _{-29.16} | 60.65 _{-16.60} | 52.63 _{-24.60} | 63.88 _{-13.70} |
| ViT-B/32-MAE [185] | 84.21 _{-3.97} | 82.96 _{-6.92} | 81.20 _{-5.69} | 81.60 _{-4.20} | 49.51 _{-28.61} | 60.23 _{-17.02} | 52.90 _{-24.33} | 63.94 _{-13.64} |
| ViT-B/32-MoCo v3 [186] | 83.97 _{-4.21} | 82.78 _{-7.10} | 80.88 _{-6.01} | 81.39 _{-4.41} | 49.36 _{-28.76} | 59.95 _{-17.30} | 52.76 _{-24.47} | 63.82 _{-13.76} |
| ViT-L/32 [38] | 84.37 _{-3.81} | 83.16 _{-6.72} | 81.32 _{-5.57} | 81.65 _{-4.15} | 49.32 _{-28.80} | 60.58 _{-16.67} | 53.03 _{-24.20} | 65.04 _{-12.54} |

image patches, and then projects each patch into a fixed-length vector and sends it to the Transformer layer. The decoder gradually upsamples the obtained feature vector to the same size as the input image for prediction. Based on ViT, MAE [185] first masks random patches and tries to reconstruct them during training, which is a typical self-supervised learning method. MoCo [186] is also an unsupervised visual representation learning method which based on ViT. MoCo compares contrastive learning to the process of looking up a dictionary, and regards the dictionary as a queue and introduces the idea of momentum update.

3.4.6 Experimental Results

The experimental results of implementing detailed model implementation tricks on 2D-UNet [44] for the 2D ISIC 2018 [78] and 2D CoNIC [79] datasets and 3D-UNet [77] for the KiTS19 [142] and 3D LiTS [67] datasets are presented in Table 7 and Table 8. The results indicate that **implementing these tricks leads to more significant accuracy improvements on 2D datasets than on 3D datasets**. For instance, implementing DeepS [179], CBL_{Dice} [181], and CBL_{Tvers} [60] on 2D-UNet [44] for ISIC 2018 [78] significantly boosts model performance. However, other tricks such as $+CBL_{Focal}$, $+CBL_{WCE}$, and $+OHEM$ [184] result in reduced model performance on most evaluation metrics for both 2D datasets. These observations and conclusions hold for 2D-UNet [44] on both ISIC 2018 [78] and CoNIC [79]. Notably, these tricks were initially designed for 2D datasets and validated on 2D datasets, which explains why they do not work well on 3D datasets.

Experimental results on 3D-UNet [77] for KiTS19 [142] and 3D LiTS [67] indicate that **implementing these model implementation tricks cannot significantly improve performance**. However, CBL_{Dice} can bring performance gains of 14.56% Recall, 7.52% Dice, and 5.23% IoU, and CBL_{Tvers} can bring performance gains of 8.54% Recall, 3.86% Dice, and 2.17% IoU on setting-ii for KiTS19 [142]. Additionally, OHEM [184] can also improve model performance. The results in the last row of Table 7 show that the effect of IntNorm [100] is not as good as that of intensity normalization [108] on the 3D KiTS19 dataset. Replacing IntNorm with intensity normalization [108] leads to a reduction in the maximum performance of -17.48% Recall, -13.87% Precision, -15.05% Dice, and -21.42% IoU. **The fact that 2D**

tricks do not work well on 3D datasets highlights the need to consider the dataset format in future model designs. To make these tricks work on 3D datasets, they may need to be revised before deployment in the application process.

The experimental results presented in Table 9 show that the performance of Transformer-based methods on ISIC 2018 [78] and CoNIC [81] is significantly lower than that of CNN-based methods. This may be because Transformer-based models lack sufficient inductive bias, and the amount of data in the training set is insufficient. In medical images, the target positions are relatively consistent, making inductive bias crucial in MedISeg. Furthermore, Transformer-based models typically have more parameters than their CNN-based counterparts, requiring a larger amount of data to optimize them. **These findings emphasize the importance of considering the amount of data available or modifying existing Transformer models to achieve satisfactory results in MedISeg.**

3.5 Model Inference

In our work, we mainly explore two kinds of commonly used inference tricks, namely, test time augmentation (TTA) and the model ensemble (Ensemble).

3.5.1 TTA

TTA can be used to improve performance without training, so it has the potential to be a plug-and-play. At the same time, it can improve the ability of model calibration, which is beneficial for visual tasks [198], [199]. In this work, we follow the same image augmentation strategy as in subsection 3.3 by three aspects: 1) implementing the TTA strategy on the baseline model (*i.e.*, $TTA_{baseline}$). 2) implementing the test time augmentation GTAug-A on the baseline model under the same data augmentation strategy GTAug-A (*i.e.*, $TTA_{GTAug-A}$). 3) implementing the test time augmentation GTAug-B on the baseline model under the same data augmentation strategy GTAug-B (*i.e.*, $TTA_{GTAug-B}$).

3.5.2 Ensemble

The commonly used model ensemble methods are voting, averaging, stacking, and non-cross-stacking (blending) [116], [197]. In our work, we first independently conduct 5 training sets with different random seeds (*i.e.*,

TABLE 10

Experimental results on model inference tricks. “All” denotes that both TTA_{GTAug} and the corresponding model ensemble strategy are used.

| Methods | Recall (%) | Precision (%) | Dice (%) | IoU (%) | Recall (%) | Precision (%) | Dice (%) | IoU (%) |
|--------------------------|-------------------------|------------------------|-------------------------|-------------------------|--------------------------|-------------------------|-------------------------|------------------------|
| 2D-UNet [44] | ISIC 2018 [78] | | | | CoNIC [81] | | | |
| | 88.18 | 89.88 | 86.89 | 85.80 | 78.12 | 77.25 | 77.23 | 77.58 |
| + $TTA_{baseline}$ | 88.55 ^{+0.37} | 90.29 ^{+0.41} | 87.42 ^{+0.53} | 86.26 ^{+0.46} | 79.13 ^{+1.01} | 80.62 ^{+3.37} | 79.37 ^{+2.14} | 79.41 ^{+1.83} |
| + $TTA_{GTAug-A}$ | 88.28 ^{+0.10} | 90.46 ^{+0.58} | 87.37 ^{+0.48} | 86.13 ^{+0.33} | 80.19 ^{+2.07} | 80.57 ^{+3.32} | 80.00 ^{+2.77} | 79.86 ^{+2.28} |
| + $TTA_{GTAug-B}$ | 90.21 ^{+2.03} | 90.94 ^{+1.06} | 88.94 ^{+2.05} | 87.59 ^{+1.79} | 80.04 ^{+1.92} | 83.81 ^{+6.56} | 81.32 ^{+4.09} | 81.22 ^{+3.64} |
| + EnsAvg [197] | 91.08 ^{+2.90} | 89.50 ^{-0.38} | 88.52 ^{+1.63} | 87.21 ^{+1.41} | 79.97 ^{+1.85} | 79.90 ^{+2.65} | 79.45 ^{+2.22} | 79.85 ^{+2.27} |
| + EnsVot [197] | 91.04 ^{+2.86} | 89.41 ^{-0.47} | 88.46 ^{+1.57} | 87.15 ^{+1.35} | 80.22 ^{+2.10} | 79.42 ^{+2.17} | 79.34 ^{+2.11} | 79.73 ^{+2.15} |
| + All (TTA_{EnsAvg}) | 88.64 ^{+0.46} | 90.96 ^{+1.08} | 87.90 ^{+1.01} | 86.72 ^{+0.92} | 79.98 ^{+1.86} | 80.60 ^{+3.35} | 79.83 ^{+2.60} | 80.15 ^{+2.57} |
| + All (TTA_{EnsVot}) | 88.61 ^{+0.43} | 90.86 ^{+0.98} | 87.87 ^{+0.98} | 86.69 ^{+0.89} | 79.89 ^{+1.77} | 80.56 ^{+3.31} | 79.76 ^{+2.53} | 80.09 ^{+2.51} |
| 3D-UNet [77] | KiTS19 [80]: settings-i | | | | KiTS19 [80]: settings-ii | | | |
| | 91.01 | 95.20 | 92.50 | 87.35 | 27.35 | 46.71 | 29.63 | 21.51 |
| + $TTA_{baseline}$ | 72.94 ^{-18.07} | 97.82 ^{+2.62} | 81.38 ^{-11.12} | 72.08 ^{-15.27} | 19.70 ^{-7.65} | 39.60 ^{-7.11} | 21.81 ^{-7.82} | 15.39 ^{-6.12} |
| + $TTA_{GTAug-A}$ | 71.32 ^{-19.69} | 97.81 ^{+2.61} | 80.22 ^{-12.28} | 70.60 ^{-16.75} | 17.20 ^{-10.15} | 38.28 ^{-8.43} | 19.16 ^{-10.47} | 13.27 ^{-8.24} |
| + $TTA_{GTAug-B}$ | 82.43 ^{-8.58} | 94.91 ^{-0.29} | 86.65 ^{-5.85} | 79.24 ^{-8.11} | 10.59 ^{-16.76} | 34.69 ^{-12.02} | 14.17 ^{-15.46} | 9.52 ^{-11.99} |
| + EnsAvg [197] | 93.00 ^{+1.99} | 96.69 ^{+1.49} | 94.39 ^{+1.89} | 90.02 ^{+2.67} | 27.09 ^{-0.26} | 54.71 ^{+8.00} | 29.15 ^{-0.48} | 21.26 ^{-0.25} |
| + EnsVot [197] | 92.90 ^{+1.89} | 96.62 ^{+1.42} | 94.31 ^{+1.81} | 89.87 ^{+2.52} | 27.65 ^{+0.30} | 56.65 ^{+9.94} | 29.44 ^{-0.19} | 21.40 ^{-0.11} |
| + All (TTA_{EnsAvg}) | 79.75 ^{-11.26} | 98.54 ^{+3.34} | 86.86 ^{-5.64} | 79.01 ^{-8.34} | 24.49 ^{-2.86} | 48.17 ^{+1.46} | 27.02 ^{-2.61} | 19.56 ^{-1.95} |
| + All (TTA_{EnsVot}) | 79.03 ^{-11.98} | 98.73 ^{+3.53} | 86.31 ^{-6.19} | 78.28 ^{-9.07} | 23.38 ^{-3.97} | 50.05 ^{+3.34} | 26.42 ^{-3.21} | 19.11 ^{-2.40} |

TABLE 11

Experimental results on 3D LiTS dataset [67] on model inference tricks. “All” denotes that both TTA_{GTAug} and the corresponding model ensemble strategy are used.

| Methods | Recall (%) | Precision (%) | Dice (%) | IoU (%) |
|--------------------------|------------------------|------------------------|------------------------|------------------------|
| 3D-UNet [77] | 89.33 | 84.03 | 86.11 | 76.44 |
| + $TTA_{baseline}$ | 81.03 ^{-8.30} | 85.35 ^{+1.32} | 82.32 ^{-3.79} | 70.81 ^{-5.63} |
| + $TTA_{GTAug-A}$ | 82.32 ^{-7.01} | 85.28 ^{+1.25} | 83.06 ^{-3.05} | 71.45 ^{-4.99} |
| + $TTA_{GTAug-B}$ | 84.82 ^{-4.51} | 83.48 ^{-0.55} | 83.38 ^{-2.73} | 72.42 ^{-4.02} |
| + EnsAvg [197] | 90.21 ^{+0.88} | 88.39 ^{+4.36} | 88.77 ^{+2.66} | 80.73 ^{+4.29} |
| + EnsVot [197] | 90.12 ^{+0.79} | 87.18 ^{+3.15} | 88.09 ^{+1.98} | 79.61 ^{+3.17} |
| + All (TTA_{EnsAvg}) | 84.16 ^{-5.17} | 88.23 ^{+4.20} | 85.46 ^{-0.65} | 75.52 ^{-0.92} |
| + All (TTA_{EnsVot}) | 84.16 ^{-5.17} | 87.70 ^{+3.67} | 85.19 ^{-0.92} | 75.05 ^{-1.39} |

2022 – 2026) obtaining 5 different models in fold-validation. Then, we choose the commonly used voting and averaging as the model ensemble strategies [197], termed as EnsVot and EnsAvg, respectively.

3.5.3 Experimental Results

Experiments are conducted on 2D-UNet [44] and 3D-UNet [77], and the results are presented in Table 10 and Table 11. The results demonstrate that **these tricks can significantly improve overall performance for 2D-UNet [44] on ISIC 2018 [78] and CoNIC [79], but not all of them are beneficial for 3D-UNet [77] on KiTS19 [80] and LiTS [67].** Among these tricks, $TTA_{GTAug-B}$ results in the maximum performance improvements, while $TTA_{GTAug-A}$ has the minimum performance improvements on average. Specifically, +EnsVot and +EnsAvg have small performance reductions on Precision by -0.38% and -0.47% , respectively.

Compared to results on ISIC 2018 [78] without using data augmentation, models using data augmentation show similar performance gains. Regarding the model ensemble on ISIC 2018 [78], both EnsAvg [197] and EnsVot [197] improve model performance by 0.46% Recall, 1.08% Precision, 1.01% Dice, and 0.92% IoU, and 0.43% Recall, 0.98% Precision, 0.98% Dice, and 0.89% IoU, respectively.

Regarding the experimental results on 2D-UNet [44] using the CoNIC [79] dataset, **we observe improvements in all evaluation metrics, strongly demonstrating the impact of test time augmentation and model ensemble on medical image segmentation tasks [166], [170], [200], [201].** However, compared to the experimental results of the baseline model on KiTS19 [80] and LiTS [67], results with TTA do not show significant improvements. The 3D setting model achieves the best performance of 93.00%, 98.73%, 94.39%, and 90.02% on Recall, Precision, Dice, and IoU on setting-i on KiTS19 [80], respectively. The 3D setting model also achieves the best performance of 27.65%, 56.65%, 29.44%, and 21.40% on Recall, Precision, Dice, and IoU on setting-i on LiTS [67], respectively. From results on 3D-UNet [77] on KiTS19 [80] and LiTS [67], we can reach the same conclusions as in subsection 3.3.

3.6 Result Post-Processing

Post-processing operations aim to enhance model performance via non-learnable approaches. For instance, segmentation results can be refined by integrating global image information. In this paper, we investigate two commonly used post-processing schemes in medical image analysis: all-but-largest-component-suppression (ABL-CS) [202] and removal of small areas (RSA) [203].

TABLE 12

Experimental results on post-processing tricks. “ABL-CS” and “RSA” denotes all-but-largest-component-suppression strategy [204] and remove small area strategy [203], respectively.

| Methods | Recall (%) | Percision (%) | Dice (%) | IoU (%) | Recall (%) | Percision (%) | Dice (%) | IoU (%) | |
|--------------|-------------------------|------------------------|------------------------|------------------------|--------------------------|------------------------|------------------------|------------------------|------------------------|
| 2D-UNet [44] | ISIC 2018 [78] | | | | CoNIC [81] | | | | |
| | 88.18 | 89.88 | 86.89 | 85.80 | 78.12 | 77.25 | 77.23 | 77.58 | |
| | + ABL-CS [205] | 87.64 _{-0.54} | 90.57 _{+0.69} | 86.99 _{+0.10} | 86.00 _{+0.20} | - | - | - | - |
| + RSA [203] | 88.15 _{-0.03} | 89.87 _{-0.01} | 86.91 _{+0.02} | 85.83 _{+0.03} | 78.00 _{-0.12} | 77.33 _{+0.08} | 77.23 _{+0.00} | 77.58 _{+0.00} | |
| 3D-UNet [77] | KiTS19 [80]: settings-i | | | | KiTS19 [80]: settings-ii | | | | |
| | 91.01 | 95.20 | 92.50 | 87.35 | 27.35 | 46.71 | 29.63 | 21.51 | |
| | + ABL-CS [205] | 90.04 _{-0.97} | 95.63 _{+0.43} | 92.14 _{-0.36} | 86.81 _{-0.54} | 23.49 _{-3.86} | 49.00 _{+2.29} | 28.23 _{-1.40} | 21.26 _{-0.25} |
| | + RSA [203] | 90.76 _{-0.25} | 95.33 _{+0.13} | 92.41 _{-0.09} | 87.22 _{-0.13} | 26.82 _{-0.53} | 44.30 _{-2.41} | 29.20 _{-0.43} | 21.36 _{-0.14} |

TABLE 13

Experimental results on 3D LiTS dataset [67] on post-processing tricks. “ABL-CS” and “RSA” denotes all-but-largest-component-suppression strategy [204] and remove small area strategy [203], respectively.

| Methods | Recall (%) | Percision (%) | Dice (%) | IoU (%) |
|----------------|------------------------|------------------------|------------------------|------------------------|
| 3D-UNet [77] | 89.33 | 84.03 | 86.11 | 76.44 |
| + ABL-CS [205] | 89.31 _{-0.02} | 87.38 _{+3.35} | 87.79 _{+1.68} | 79.13 _{+2.69} |
| + RSA [203] | 89.32 _{-0.01} | 84.19 _{+0.16} | 86.19 _{+0.08} | 76.58 _{+0.14} |

3.6.1 ABL-CS

ABL-CS [202] aims to remove some wrong areas in the segmentation results based on knowledge of the organism’s physical properties [204]. For example, for the heart segmentation task, we all know that every person has only one heart, so if there are small segmentation areas in the obtained mask, we need to remove this small areas [205].

3.6.2 RSA

For MediSeg, the imaging protocol is generally unchanged, such that the area of each instance segmentation mask remains unvaried as well. Based on this physical property, we can set a pixel-level threshold to remove some instance masks that are too small (*i.e.*, under the given threshold) in the obtained segmentation masks [203]. In our work, following [206], [207], the threshold is set to 5000 for setting-i, 80 for for setting-ii, 120 for ISIC 2018 [78], and 10 for CoNIC [79] and LiTS [67]. This means that all masks in the segmented area with less than this threshold are eliminated from the final results.

3.6.3 Experimental Results

Experiments for post-processing strategies are carried out on 2D-UNet [44] for ISIC 2018 [78] and CoNIC [79] datasets, and 3D-UNet [77] for KiTS19 [142] and LiTS [67] datasets, respectively. Results are shown in Table 12 and Table 13. We can observe that compared to the baseline 2D-UNet on ISIC 2018 [78], implementing ABL-CS on the baseline model can boost three-quarters of the evaluation metrics. For example, 0.69% Precision, 0.10% Dice, and 0.20% IoU. Implementing RSA on the baseline model can boost 0.02% Dice, and 0.03% IoU. We can also observe that +RSA has a weak effect on performance improvements on ISIC 2018 [78], *e.g.*, the increased model performance is almost always less than 0.1%. Since ABL-CS does not apply to the CoNIC [79] dataset, we only implement RSA on CoNIC [79]. We can observe that values

under these evaluation metrics have very little changes. The experimental results on 3D-UNet [77] on KiTS19 [142] show that + ABL-CS can improve model performance on Precision by 0.43% and 2.29% on setting-i and setting-ii, respectively. Besides, + RSA only works on setting-i by improving 0.13% Precision. **The above experimental results of + ABL-CS and + RSA on the 3D setting on KiTS19 [142] demonstrate that these two post-processing schemes are ineffective in improving performance for Recall, Dice, and IoU.** The experimental results on LiTS [67] show that these two schemes can improve all evaluation metrics except Recall. These experimental results show that the performance of the same post-processing operation on different datasets and different evaluation metrics is also different. It also shows us that we need to pay attention to the state of the datasets when choosing the post-processing tricks, and to what evaluation metrics we are focusing on.

4 DISCUSSIONS

In this section, we discuss the potential challenges and problems corresponding to the above experimental tricks. In addition, we also point out the limitations of these tricks. As illustrated in Figure 2, an unabridged MediSeg system can be separated into six main implementation phases. We collected and explored a series of tricks in each phase. The potential challenges we addressed included but not limited to **small dataset**, **class imbalance learning**, **multi-modality learning**, and **domain adaptation**.

4.1 Challenges

By incorporating the collected tricks into various baseline models, we observed significant improvements in performance. It is worth noting that while these enhancements can be attributed to the implementation of the tricks on the baselines, the performance gains are also attributable to the underlying fundamental challenges posed by medical image processing problems themselves. Despite differences in deployment and appearance, the problems addressed by the tricks share similar objectives with advanced approaches. For instance, we observed that fine-tuning pre-trained weights can lead to substantial enhancements in model performance (*ref.* Table 1 and Table 2). First, this observation demonstrates that the pre-trained weights on the natural scenes can be transferred into the medical scene via a plain fine-tuning strategy, thereby essentially

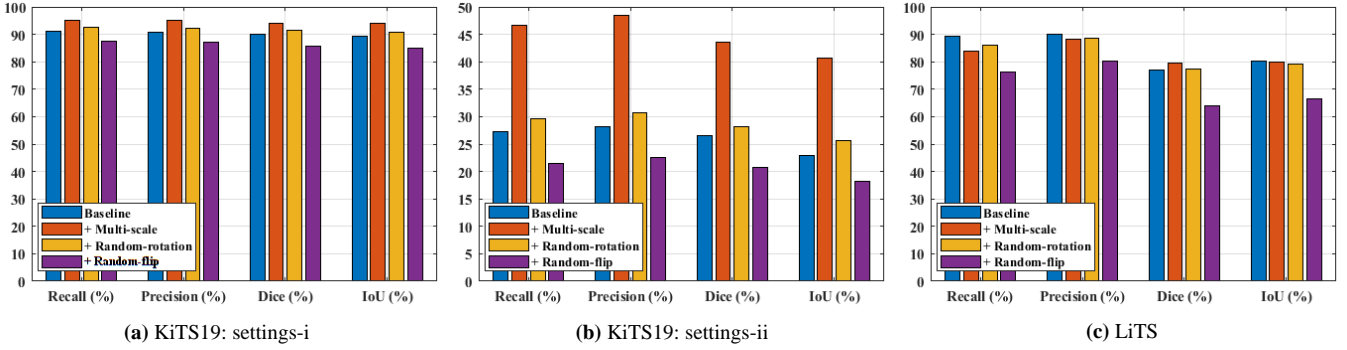


Fig. 3. The segmentation result illustrations by adding each single data augmentation scheme on 3D KiTS19 [80] and LiTS [67] datasets, respectively. The baseline model is 3D-UNet [77]. (a) the foreground “kidney” and the “background” in KiTS19 [80], (b) the foreground “tumor” and the “background” in KiTS19 [80], (c) the foreground “liver” and the “background” in LiTS [67].

solves **multi-modality learning** and **domain adaptation** (i.e., cross-domain representations between natural scenarios and medical scenarios) problems. Although these problems can also be solved by some advanced transfer learning [208]–[210] or meta-learning approaches [200], [211], fine-tuning is a cheap solution. Second, it shows that training on more data samples helps to improve the model performance, which corresponds to problems of **small dataset** and overfitting. These two problems are accentuated in models with very strong learning capabilities (e.g., the transformer-based models), as such models generally require very large datasets to train.

In addition to the pre-training model, observations and conclusions can also be made on data pre-processing, data augmentation, and test time augmentation, as shown in Table 3 to Table 13. Data pre-processing and data augmentation methods can enhance the experimental dataset representation ability, implicitly addressing challenges posed by insufficient training samples, **small dataset**, and **class imbalance learning**. Patching, OverSam, and ReSam methods are effective in mitigating these challenges. In particular, Patching and OverSam can be used to address **small dataset**, while Patching, OverSam, ReSam, and IntesNorm can be employed to address **class imbalance learning**. Fortunately, these methods do not incur significant computational costs and can be implemented seamlessly. While data augmentation and test time augmentation may not always improve performance, this may be due to dataset-specific factors rather than limitations of the techniques themselves.

In addition, there are significant differences between individual geometric transformation-based data augmentation schemes. Segmentation illustrations of each data augmentation scheme on KiTS19 [142] and LiTS [67] are visualized in Figure 3. Multiple scales and rotation improve model performance on some evaluation metrics for KiTS19 [142], while the use of flip markedly reduces the model performance. Results on LiTS [67] show that multi-scale only improves a portion of the evaluation metrics (e.g., Dice), and the remaining data augmentation schemes do not work. These results validate our hypothesis that data augmentation methods with non-destructive inductive biases (e.g., multi-scale) are more beneficial for images with relatively fixed object positions. GAN-based data augmentation methods can improve dataset representation without

destroying such inductive biases, achieving better performance on KiTS19 [142] (see Table 5). These experiments suggest that future data augmentation designs should consider the specific state (e.g., modality, distribution, and lesion size) of the dataset used. Additionally, **class imbalance learning** can also be addressed using the collected tricks (see Table 7 and Table 8). In summary, our work provides not only a completed MediSeg survey but also a practical guide for addressing segmentation-related challenges in medical image processing, including but not limited to **small dataset**, **class imbalance learning**, **multi-modality learning**, and **domain adaptation**.

4.2 Limitations

There are some limitations of this work. For example, the collected tricks are limited, meaning that the tricks collected and experimented with in our paper are only a finite subset of all the medical image segmentation tricks. This point can be elaborated into the following two aspects:

(1) **Surveyed Subset of Tricks:** We only collected a representative number of tricks for the same category of phase. For example, there exist many data augmentation schemes such as translating, color jittering, contrast, simulation of low resolution, Gaussian noise injection, mixing images, random erasing, Gaussian blur, mixup, and cutmix [59], [166], [168], [170], [190]. However, due to the practical requirements of medical image processing and the characteristics of the experimental datasets, only a small number of these techniques were used.

(2) **Limited Application of Surveyed Tricks:** In our work, we chose commonly used 2D-UNet [44] and 3D-UNet [77] as our baseline models and validated the effectiveness of these tricks on four representative 2D and 3D medical image datasets. However, there are a large number of progressive MediSeg models with different backbones at different levels that were not involved.

(3) **Limited Effect of Surveyed Tricks:** Medical image processing is closely related to clinical practice and involves many complex challenging problems, such as sheltered objects [212], blurred images [213], the long-tail problem [214], incremental learning problem in medical images [215], and object boundary detection and refinement [2]. In our work, we only addressed some of the fundamental challenges.

Overall, our work provides a useful starting point for exploring a subset of medical image segmentation tricks, but further investigation is needed to fully explore the potential of these techniques in medical image processing.

5 CONCLUSIONS AND FUTURE DIRECTIONS

In this work, we have collected a comprehensive set of MedISeg tricks that cover common and fundamental schemes used in medical image segmentation. To avoid performance ambiguity from implementation variations, we experimentally explored the effectiveness of these tricks on consistent 2D-UNet [44] and 3D-UNet [77] baseline models. Our experiments on 2D ISIC 2018 [78], 2D CoNIC [79], [81], [101], 3D KiTS19 [80] and 3D LiTS [67] datasets have shown the effectiveness of these tricks and helped us provide empirical guidance for the forthcoming segmentation pipelines, including network architectures, training strategies, and loss functions.

One of the important contributions of our work is the explicit exploration of the effect of these collected tricks. Our work not only promotes subsequent methods to pay attention to tricks but also achieves a fair result comparison. This is especially necessary as network architectures become more sophisticated in the face of complex tasks such as image segmentation [188], [192], object detection [47], [182], and image generation [83], [120]. Compared to existing paper-driven segmentation surveys [10], [83], [151], [152], [166], [170], [177], [201] that only blandly focus on advantage and limitation analyses, our work provides extensive experiments and is more technically operable.

In the future, we plan to work in the following directions:

5.1 Trick Track

(1) Survey and develop more tricks on MedISeg. As MedISeg is closely integrated with clinical practice, it is of great practical value to continue exploring and developing more advanced MedISeg tricks to meet the requirements of different problems.

(2) Explore the effectiveness of tricks on more methods and datasets. To enable a more comprehensive and fair comparison of experimental results, it is necessary to conduct a thorough trick survey. This is especially important when faced with MedISeg problems where different image types, distributions, and inner class divergence can affect the effectiveness of a specific trick.

(3) Explore trick-inspired model designs. Although tricks are often overlooked in existing publications, the principles and ideas they contain can inspire subsequent work to achieve cheaper and more computationally friendly model designs.

(4) Explore attention-based tricks. With the multi-head attention mechanism providing a strong feature representation ability, the visual transformer framework has received more attention in communities of computer vision and medical image analysis. However, due to its complex internal architectures and immature practice applications (especially in the face of small datasets), there is a need to explore trick research on the vision transformer framework.

5.2 After Large Vision Models

Recently, there has been a surge of interest in large vision models, such as SAM [216] and MedSAM [217], which have ushered in a new era of image semantic recognition, particularly for dense image predictions, such as semantic segmentation and instance segmentation [218], [219]. These models have enabled breakthrough progress and impressive performance on challenging tasks of images of natural scenes, such as image inpainting and camouflaged object detection [218]–[223]. However, there still exists a gap between the performance of large vision models on specific medical datasets and that of state-of-the-art models [224]–[227]. Therefore, it is imperative to explore integrate off-the-shelf large vision models with downstream medical image processing tasks and achieve satisfactory results on specific medical image datasets. Moreover, there is great potential in combining large vision models with large vision-language models (e.g., ChatCAD [228] and CLIP [229]) in the domain of medical image analysis. This could involve designing efficient visual prompts [230] or visual adapters [231] that would enable the resulting models to be deployed on edge computing devices. This promising research direction could lead to significant advancements in MedISeg and other medical image analysis tasks.

REFERENCES

- [1] C. J. Lynch and C. Liston, "New machine-learning technologies for computer-aided diagnosis," *Nature Medicine*, vol. 24, no. 9, pp. 1304–1305, 2018.
- [2] R. Wang, S. Chen, C. Ji, J. Fan, and Y. Li, "Boundary-aware context neural network for medical image segmentation," *Medical Image Analysis*, vol. 78, p. 102395, 2022.
- [3] R. Azad, N. Khosravi, M. Dehghanmanshadi, J. Cohen-Adad, and D. Merhof, "Medical image segmentation on mri images with missing modalities: A review," *arXiv*, 2022.
- [4] G. Wang, M. A. Zuluaga, W. Li, R. Pratt, P. A. Patel, M. Aertsen, T. Doel, A. L. David, J. Deprest, S. Ourselin *et al.*, "Deepigeos: a deep interactive geodesic framework for medical image segmentation," *IEEE Transactions on Pattern Analysis and Machine Intelligence*, vol. 41, no. 7, pp. 1559–1572, 2018.
- [5] D. Shen, G. Wu, and H.-I. Suk, "Deep learning in medical image analysis," *Annual Review of Biomedical Engineering*, vol. 19, p. 221, 2017.
- [6] W. Zhu, L. Sun, J. Huang, L. Han, and D. Zhang, "Dual attention multi-instance deep learning for alzheimer's disease diagnosis with structural mri," *IEEE Transactions on Medical Imaging*, vol. 40, no. 9, pp. 2354–2366, 2021.
- [7] M. Liu, D. Zhang, and D. Shen, "Relationship induced multi-template learning for diagnosis of alzheimer's disease and mild cognitive impairment," *IEEE Transactions on Medical Imaging*, vol. 35, no. 6, pp. 1463–1474, 2016.
- [8] X. Li, H. Chen, X. Qi, Q. Dou, C.-W. Fu, and P. A. Heng, "H-denseunet: hybrid densely connected unet for liver and tumor segmentation from ct volumes," *IEEE Transactions on Medical Imaging*, vol. 37, no. 12, pp. 2663–2674, 2018.
- [9] T. Liu, E. Siegel, and D. Shen, "Deep learning and medical image analysis for covid-19 diagnosis and prediction," *Annual Review of Biomedical Engineering*, vol. 24, 2022.
- [10] K. Munir, H. Elahi, A. Ayub, F. Frezza, and A. Rizzi, "Cancer diagnosis using deep learning: a bibliographic review," *Cancers*, vol. 11, no. 9, pp. 1235–1246, 2019.
- [11] C. Jin, H. Yu, J. Ke, P. Ding, Y. Yi, X. Jiang, X. Duan, J. Tang, D. T. Chang, X. Wu *et al.*, "Predicting treatment response from longitudinal images using multi-task deep learning," *Nature Communications*, vol. 12, no. 1, pp. 1–11, 2021.
- [12] D. L. Pham, C. Xu, and J. L. Prince, "Current methods in medical image segmentation," *Annual Review of Biomedical Engineering*, vol. 2, no. 1, pp. 315–337, 2000.

- [13] R. H. Taylor, "Computer-integrated interventional medicine: A 30 year perspective," in *Medical Image Computing and Computer Assisted Intervention (MICCAI)*, 2020.
- [14] J. Fu, J. Liu, H. Tian, Y. Li, Y. Bao, Z. Fang, and H. Lu, "Dual attention network for scene segmentation," in *IEEE Conference on Computer Vision and Pattern Recognition (CVPR)*, 2019.
- [15] D. Zhang, Y. Sun, Q. Ye, and J. Tang, "Recursive discriminative subspace learning with l1-norm distance constraint," *IEEE Transactions on Cybernetics*, vol. 50, no. 5, pp. 2138–2151, 2018.
- [16] X. Lu, W. Wang, C. Ma, J. Shen, L. Shao, and F. Porikli, "See more, know more: Unsupervised video object segmentation with co-attention siamese networks," in *IEEE Conference on Computer Vision and Pattern Recognition (CVPR)*, 2019.
- [17] J. Long, E. Shelhamer, and T. Darrell, "Fully convolutional networks for semantic segmentation," in *IEEE Conference on Computer Vision and Pattern Recognition (CVPR)*, 2015.
- [18] K. He, X. Zhang, S. Ren, and J. Sun, "Deep residual learning for image recognition," in *IEEE Conference on Computer Vision and Pattern Recognition (CVPR)*, 2016.
- [19] H. Chen, Q. Dou, L. Yu, J. Qin, and P. A. Heng, "Voxresnet: Deep voxelwise residual networks for brain segmentation from 3d mr images," *NeuroImage*, vol. 170, no. 1, pp. 446–455, 2018.
- [20] Y. Lin, D. Zhang, X. Fang, Y. Chen, K.-T. Cheng, and H. Chen, "Rethinking boundary detection in deep learning models for medical image segmentation," *arXiv*, 2023.
- [21] X. Yang, C. Liu, Z. Wang, J. Yang, H. Le Min, L. Wang, and K. T. T. Cheng, "Co-trained convolutional neural networks for automated detection of prostate cancer in multi-parametric mri," *Medical Image Analysis*, vol. 42, no. 1, pp. 212–227, 2017.
- [22] D. Zhang, Y. Wang, L. Zhou, H. Yuan, D. Shen, A. D. N. Initiative *et al.*, "Multimodal classification of alzheimer's disease and mild cognitive impairment," *Neuroimage*, vol. 55, no. 3, pp. 856–867, 2011.
- [23] W. Zhang, R. Li, H. Deng, L. Wang, W. Lin, S. Ji, and D. Shen, "Deep convolutional neural networks for multi-modality iso-intense infant brain image segmentation," *NeuroImage*, vol. 108, pp. 214–224, 2015.
- [24] H.-I. Suk, S.-W. Lee, D. Shen, A. D. N. Initiative *et al.*, "Hierarchical feature representation and multimodal fusion with deep learning for ad/mci diagnosis," *NeuroImage*, vol. 101, pp. 569–582, 2014.
- [25] D. Zhang, D. Shen, A. D. N. Initiative *et al.*, "Multi-modal multi-task learning for joint prediction of multiple regression and classification variables in alzheimer's disease," *NeuroImage*, vol. 59, no. 2, pp. 895–907, 2012.
- [26] F. Shan, Y. Gao, J. Wang, W. Shi, N. Shi, M. Han, Z. Xue, D. Shen, and Y. Shi, "Lung infection quantification of covid-19 in ct images with deep learning," *arXiv*, 2020.
- [27] R. Ge, Y. He, C. Xia, C. Xu, W. Sun, G. Yang, J. Li, Z. Wang, H. Yu, D. Zhang *et al.*, "X-ctrnsnet: 3d cervical vertebra ct reconstruction and segmentation directly from 2d x-ray images," *Knowledge-Based Systems*, vol. 236, p. 107680, 2022.
- [28] L. Chen, G. Papandreou, F. Schroff, and H. Adam, "Rethinking atrous convolution for semantic image segmentation," *arXiv*, 2017.
- [29] C. Szegedy, W. Liu, Y. Jia, P. Sermanet, S. Reed, D. Anguelov, D. Erhan, V. Vanhoucke, and A. Rabinovich, "Going deeper with convolutions," in *IEEE Conference on Computer Vision and Pattern Recognition (CVPR)*, 2015.
- [30] G. Huang, Z. Liu, L. Van Der Maaten, and K. Q. Weinberger, "Densely connected convolutional networks," in *IEEE Conference on Computer Vision and Pattern Recognition (CVPR)*, 2017.
- [31] A. Krizhevsky, I. Sutskever, and G. E. Hinton, "Imagenet classification with deep convolutional neural networks," in *Advances in Neural Information Processing Systems (NeurIPS)*, 2012.
- [32] K. Simonyan and A. Zisserman, "Very deep convolutional networks for large-scale image recognition," in *International Conference on Learning Representations (ICLR)*, 2015.
- [33] A. G. Howard, M. Zhu, B. Chen, D. Kalenichenko, W. Wang, T. Weyand, M. Andreetto, and H. Adam, "Mobilenets: Efficient convolutional neural networks for mobile vision applications," *arXiv*, 2017.
- [34] X. Zhang, X. Zhou, M. Lin, and J. Sun, "Shufflenet: An extremely efficient convolutional neural network for mobile devices," in *IEEE Conference on Computer Vision and Pattern Recognition (CVPR)*, 2018.
- [35] S. Xie, R. Girshick, P. Dollár, Z. Tu, and K. He, "Aggregated residual transformations for deep neural networks," in *IEEE Conference on Computer Vision and Pattern Recognition (CVPR)*, 2017.
- [36] J. Wang, K. Sun, T. Cheng, B. Jiang, C. Deng, Y. Zhao, D. Liu, Y. Mu, M. Tan, X. Wang *et al.*, "Deep high-resolution representation learning for visual recognition," *IEEE Transactions on Pattern Analysis and Machine Intelligence*, vol. 43, no. 10, pp. 3349–3364, 2020.
- [37] I. Radosavovic, R. P. Kosaraju, R. Girshick, K. He, and P. Dollár, "Designing network design spaces," in *IEEE Conference on Computer Vision and Pattern Recognition (CVPR)*, 2020.
- [38] A. Dosovitskiy, L. Beyer, A. Kolesnikov, D. Weissenborn, X. Zhai, T. Unterthiner, M. Dehghani, M. Minderer, G. Heigold, S. Gelly *et al.*, "An image is worth 16x16 words: Transformers for image recognition at scale," in *International Conference on Learning Representations (ICLR)*, 2021.
- [39] Z. Liu, Y. Lin, Y. Cao, H. Hu, Y. Wei, Z. Zhang, S. Lin, and B. Guo, "Swin transformer: Hierarchical vision transformer using shifted windows," in *IEEE/CVF International Conference on Computer Vision (ICCV)*, 2021.
- [40] J. Guo, K. Han, H. Wu, Y. Tang, X. Chen, Y. Wang, and C. Xu, "Cmt: Convolutional neural networks meet vision transformers," in *IEEE Conference on Computer Vision and Pattern Recognition (CVPR)*, 2022.
- [41] Z. Peng, W. Huang, S. Gu, L. Xie, Y. Wang, J. Jiao, and Q. Ye, "Conformer: Local features coupling global representations for visual recognition," in *IEEE/CVF International Conference on Computer Vision (ICCV)*, 2021.
- [42] H. Wu, B. Xiao, N. Codella, M. Liu, X. Dai, L. Yuan, and L. Zhang, "Cvt: Introducing convolutions to vision transformers," in *IEEE/CVF International Conference on Computer Vision (ICCV)*, 2021.
- [43] V. Badrinarayanan, A. Kendall, and R. Cipolla, "Segnet: A deep convolutional encoder-decoder architecture for image segmentation," *IEEE Transactions on Pattern Analysis and Machine Intelligence*, vol. 39, no. 12, pp. 2481–2495, 2017.
- [44] O. Ronneberger, P. Fischer, and T. Brox, "U-net: Convolutional networks for biomedical image segmentation," in *Medical Image Computing and Computer Assisted Intervention (MICCAI)*, 2015.
- [45] X. Guan, G. Yang, J. Ye, W. Yang, X. Xu, W. Jiang, and X. Lai, "3d agse-vnet: an automatic brain tumor mri data segmentation framework," *BMC Medical Imaging*, vol. 22, no. 1, pp. 1–18, 2022.
- [46] Y. Quan, D. Zhang, L. Zhang, and J. Tang, "Centralized feature pyramid for object detection," *arXiv*, 2022.
- [47] T. Y. Lin, P. Dollár, R. Girshick, K. He, B. Hariharan, and S. Belongie, "Feature pyramid networks for object detection," in *IEEE Conference on Computer Vision and Pattern Recognition (CVPR)*, 2017.
- [48] C. Wang, D. Zhang, L. Zhang, and J. Tang, "Coupling global context and local contents for weakly-supervised semantic segmentation," *arXiv*, 2023.
- [49] X. Wang, R. Girshick, A. Gupta, and K. He, "Non-local neural networks," in *IEEE Conference on Computer Vision and Pattern Recognition (CVPR)*, 2018.
- [50] D. Zhang, C. Zuo, Q. Wu, L. Fu, and X. Xiang, "Unabridged adjacent modulation for clothing parsing," *Pattern Recognition*, vol. 127, p. 108594, 2022.
- [51] K. Nigam and R. Ghani, "Analyzing the effectiveness and applicability of co-training," in *Conference on Information and Knowledge Management (CIKM)*, 2000.
- [52] J. Peng, G. Estrada, M. Pedersoli, and C. Desrosiers, "Deep co-training for semi-supervised image segmentation," *Pattern Recognition*, vol. 107, p. 107269, 2020.
- [53] B. Han, Q. Yao, X. Yu, G. Niu, M. Xu, W. Hu, I. Tsang, and M. Sugiyama, "Co-teaching: Robust training of deep neural networks with extremely noisy labels," in *Advances in Neural Information Processing Systems (NeurIPS)*, 2018.
- [54] F. Robinet, C. Parera, C. Hundt, and R. Frank, "Weakly-supervised free space estimation through stochastic co-teaching," in *IEEE/CVF Winter Conference on Applications of Computer Vision (WACV)*, 2022.
- [55] G. Song and W. Chai, "Collaborative learning for deep neural networks," in *Advances in Neural Information Processing Systems (NeurIPS)*, 2018.
- [56] H. Wei, H. Cao, Y. Cao, Y. Zhou, W. Xue, D. Ni, and S. Li, "Temporal-consistent segmentation of echocardiography with

- co-learning from appearance and shape," in *Medical Image Computing and Computer Assisted Intervention (MICCAI)*, 2020.
- [57] A. Bartler, A. Bühler, F. Wiewel, M. Döbler, and B. Yang, "Mt3: Meta test-time training for self-supervised test-time adaption," in *International Conference on Artificial Intelligence and Statistics (AISTATS)*, 2022.
- [58] Y. Sun, X. Wang, Z. Liu, J. Miller, A. Efros, and M. Hardt, "Test-time training with self-supervision for generalization under distribution shifts," in *International Conference on Machine Learning (ICML)*, 2020.
- [59] M. Yeung, E. Sala, C.-B. Schönlieb, and L. Rundo, "Unified focal loss: Generalising dice and cross entropy-based losses to handle class imbalanced medical image segmentation," *Computerized Medical Imaging and Graphics*, vol. 95, no. 1, p. 102026, 2022.
- [60] S. S. M. Salehi, D. Erdogmus, and A. Gholipour, "Tversky loss function for image segmentation using 3d fully convolutional deep networks," in *Medical Image Computing and Computer Assisted Intervention (MICCAI)*, 2017.
- [61] T. Athanasiadis, P. Mylonas, Y. Avrithis, and S. Kollias, "Semantic image segmentation and object labeling," *IEEE Transactions on Circuits and Systems for Video Technology*, vol. 17, no. 3, pp. 298–312, 2007.
- [62] J. Ma, J. Chen, M. Ng, R. Huang, Y. Li, C. Li, X. Yang, and A. L. Martel, "Loss odyssey in medical image segmentation," *Medical Image Analysis*, vol. 71, no. 6, p. 102035, 2021.
- [63] A. Steiner, A. Kolesnikov, X. Zhai, R. Wightman, J. Uszkoreit, and L. Beyer, "How to train your vit? data, augmentation, and regularization in vision transformers," *arXiv*, 2021.
- [64] T. He, Z. Zhang, H. Zhang, Z. Zhang, J. Xie, and M. Li, "Bag of tricks for image classification with convolutional neural networks," in *IEEE Conference on Computer Vision and Pattern Recognition (CVPR)*, 2019.
- [65] Z. Shi, H. Chen, and D. Zhang, "Transformer-auxiliary neural networks for image manipulation localization by operator inductions," *IEEE Transactions on Circuits and Systems for Video Technology*, 2023.
- [66] D. Zhang, J. Tang, and K.-T. Cheng, "Graph reasoning transformer for image parsing," in *ACM International Conference on Multimedia (ACM MM)*, 2022.
- [67] P. Bilic, P. F. Christ, E. Vorontsov, G. Chlebus, H. Chen, Q. Dou, C.-W. Fu, X. Han, P. A. Heng, J. Hesser *et al.*, "The liver tumor segmentation benchmark (lits)," *arXiv*, 2019.
- [68] W. Zhang, D. Zhang, and X. Xiang, "Cascaded and dual: Discrimination oriented network for brain tumor classification," in *Asian Conference on Machine Learning (ACML)*, 2019.
- [69] Z. Shi, H. Chen, L. Chen, and D. Zhang, "Discrepancy-guided reconstruction learning for image forgery detection," *arXiv*, 2023.
- [70] Y. Li, L. Luo, H. Lin, H. Chen, and P. A. Heng, "Dual-consistency semi-supervised learning with uncertainty quantification for covid-19 lesion segmentation from ct images," in *Medical Image Computing and Computer Assisted Intervention (MICCAI)*, 2021.
- [71] H. Zhao, J. Shi, X. Qi, X. Wang, and J. Jia, "Pyramid scene parsing network," in *IEEE Conference on Computer Vision and Pattern Recognition (CVPR)*, 2017.
- [72] L. Chen, Y. Zhu, G. Papandreou, F. Schroff, and H. Adam, "Encoder-decoder with atrous separable convolution for semantic image segmentation," in *European Conference on Computer Vision (ECCV)*, 2018.
- [73] J. Hu, L. Shen, and G. Sun, "Squeeze-and-excitation networks," *IEEE Transactions on Pattern Analysis and Machine Intelligence*, vol. 42, no. 8, pp. 2011–2023, 2020.
- [74] H. Touvron, M. Cord, M. Douze, F. Massa, A. Sablayrolles, and H. Jégou, "Training data-efficient image transformers & distillation through attention," in *International Conference on Machine Learning (ICML)*, 2021.
- [75] D. Zhang, L. Zhang, and J. Tang, "Augmented fcn: rethinking context modeling for semantic segmentation," *Science China Information Sciences*, vol. 66, no. 4, p. 142105, 2023.
- [76] X. Ding, X. Zhang, N. Ma, J. Han, G. Ding, and J. Sun, "Repvgg: Making vgg-style convnets great again," in *IEEE Conference on Computer Vision and Pattern Recognition (CVPR)*, 2021.
- [77] Ö. Çiçek, A. Abdulkadir, S. S. Lienkamp, T. Brox, and O. Ronneberger, "3d u-net: learning dense volumetric segmentation from sparse annotation," in *Medical Image Computing and Computer Assisted Intervention (MICCAI)*, 2016.
- [78] N. Codella, V. Rotemberg, P. Tschandl, M. E. Celebi, S. Dusza, D. Gutman, B. Helba, A. Kallou, K. Liopyris, M. Marchetti *et al.*, "Skin lesion analysis toward melanoma detection 2018: A challenge hosted by the international skin imaging collaboration (isic)," *arXiv*, 2019.
- [79] S. Graham, M. Jahanifar, Q. D. Vu, G. Hadjigeorgiou, T. Leech, D. Snead, S. E. A. Raza, F. Minhas, and N. Rajpoot, "Conic: Colon nuclei identification and counting challenge 2022," *arXiv*, 2021.
- [80] N. Heller, F. Isensee, K. H. Maier-Hein, X. Hou, C. Xie, F. Li, Y. Nan, G. Mu, Z. Lin, M. Han *et al.*, "The state of the art in kidney and kidney tumor segmentation in contrast-enhanced ct imaging: Results of the kits19 challenge," *Medical Image Analysis*, vol. 67, p. 101821, 2021.
- [81] S. Graham, M. Jahanifar, A. Azam, M. Nimir, Y.-W. Tsang, K. Dodd, E. Hero, H. Sahota, A. Tank, K. Benes *et al.*, "Lizard: a large-scale dataset for colonic nuclear instance segmentation and classification," in *IEEE/CVF International Conference on Computer Vision (ICCV)*, 2021.
- [82] H. Cao, Y. Wang, J. Chen, D. Jiang, X. Zhang, Q. Tian, and M. Wang, "Swin-unet: Unet-like pure transformer for medical image segmentation," *arXiv*, 2021.
- [83] T. Zhou, S. Ruan, and S. Canu, "A review: Deep learning for medical image segmentation using multi-modality fusion," *Array*, vol. 3, no. 1, pp. 4–100, 2019.
- [84] A. Sinha and J. Dolz, "Multi-scale self-guided attention for medical image segmentation," *IEEE Journal of Biomedical and Health Informatics*, vol. 25, no. 1, pp. 121–130, 2020.
- [85] Y. Zhang, H. Liu, and Q. Hu, "Transfuse: Fusing transformers and cnns for medical image segmentation," in *Medical Image Computing and Computer Assisted Intervention (MICCAI)*, 2021.
- [86] S. Feng, H. Zhao, F. Shi, X. Cheng, M. Wang, Y. Ma, D. Xiang, W. Zhu, and X. Chen, "Cpfnet: Context pyramid fusion network for medical image segmentation," *IEEE Transactions on Medical Imaging*, vol. 39, no. 10, pp. 3008–3018, 2020.
- [87] V. Nair and G. E. Hinton, "Rectified linear units improve restricted boltzmann machines," in *International Conference on Machine Learning (ICML)*, 2010.
- [88] A. F. Agarap, "Deep learning using rectified linear units (relu)," *arXiv*, 2018.
- [89] P. Smith, "Bilinear interpolation of digital images," *Ultramicroscopy*, vol. 6, no. 2, pp. 201–204, 1981.
- [90] A. Hatamizadeh, Y. Tang, V. Nath, D. Yang, A. Myronenko, B. Landman, H. R. Roth, and D. Xu, "Unetr: Transformers for 3d medical image segmentation," in *IEEE/CVF Winter Conference on Applications of Computer Vision (WACV)*, 2022.
- [91] Y. Xie, J. Zhang, C. Shen, and Y. Xia, "Cotr: Efficiently bridging cnn and transformer for 3d medical image segmentation," in *Medical Image Computing and Computer Assisted Intervention (MICCAI)*, 2021.
- [92] Q. Yu, D. Yang, H. Roth, Y. Bai, Y. Zhang, A. L. Yuille, and D. Xu, "C2fnas: Coarse-to-fine neural architecture search for 3d medical image segmentation," in *IEEE Conference on Computer Vision and Pattern Recognition (CVPR)*, 2020.
- [93] X. Wang, S. Han, Y. Chen, D. Gao, and N. Vasconcelos, "Volumetric attention for 3d medical image segmentation and detection," in *Medical Image Computing and Computer Assisted Intervention (MICCAI)*, 2019.
- [94] J. Zhang, Y. Xie, Y. Wang, and Y. Xia, "Inter-slice context residual learning for 3d medical image segmentation," *IEEE Transactions on Medical Imaging*, vol. 40, no. 2, pp. 661–672, 2020.
- [95] X. Liao, W. Li, Q. Xu, X. Wang, B. Jin, X. Zhang, Y. Wang, and Y. Zhang, "Iteratively-refined interactive 3d medical image segmentation with multi-agent reinforcement learning," in *IEEE Conference on Computer Vision and Pattern Recognition (CVPR)*, 2020.
- [96] Y. Wu, K. Liao, J. Chen, D. Z. Chen, J. Wang, H. Gao, and J. Wu, "D-former: A u-shaped dilated transformer for 3d medical image segmentation," *arXiv*, 2022.
- [97] X. Yan, H. Tang, S. Sun, H. Ma, D. Kong, and X. Xie, "After-unet: Axial fusion transformer unet for medical image segmentation," in *IEEE/CVF Winter Conference on Applications of Computer Vision (WACV)*, 2022.
- [98] A. Hatamizadeh, Z. Xu, D. Yang, W. Li, H. Roth, and D. Xu, "Unetformer: A unified vision transformer model and pre-training framework for 3d medical image segmentation," *arXiv*, 2022.
- [99] S. Ji, W. Xu, M. Yang, and K. Yu, "3d convolutional neural networks for human action recognition," *IEEE Transactions on Pattern Analysis and Machine Intelligence*, vol. 35, no. 1, pp. 221–231, 2012.

- [100] S. Ioffe and C. Szegedy, "Batch normalization: Accelerating deep network training by reducing internal covariate shift," in *International Conference on Machine Learning (ICML)*, 2015.
- [101] S. Graham, Q. D. Vu, S. E. A. Raza, A. Azam, Y. W. Tsang, J. T. Kwak, and N. Rajpoot, "Hover-net: Simultaneous segmentation and classification of nuclei in multi-tissue histology images," *Medical Image Analysis*, vol. 58, p. 101563, 2019.
- [102] N. Abraham and N. M. Khan, "A novel focal tversky loss function with improved attention u-net for lesion segmentation," in *International Symposium on Biomedical Imaging (ISBI)*, 2019.
- [103] R. Azad, M. Asadi Aghbolaghi, M. Fathy, and S. Escalera, "Attention deeplabv3+: Multi-level context attention mechanism for skin lesion segmentation," in *European Conference on Computer Vision (ECCV)*, 2020.
- [104] M. Weigert and U. Schmidt, "Nuclei segmentation and classification in histopathology images with stardist for the conic challenge 2022," *arXiv*, 2022.
- [105] M. Böhland, O. Neumann, M. P. Schilling, M. Reischl, R. Mikut, K. Löffler, and T. Scherr, "ciscnet—a single-branch cell instance segmentation and classification network," *arXiv*, 2022.
- [106] C.-Y. Lee, H.-C. Chien, C.-P. Wang, H. Yen, K.-W. Zhen, and H.-K. Lin, "Using multi-scale swintransformer-htc with data augmentation in conic challenge," *arXiv*, 2022.
- [107] N. Heller, N. Sathianathan, A. Kalapara, E. Walczak, K. Moore, H. Kaluzniak, J. Rosenberg, P. Blake, Z. Rengel, M. Oestreich *et al.*, "The kits19 challenge data: 300 kidney tumor cases with clinical context, ct semantic segmentations, and surgical outcomes," *arXiv*, 2019.
- [108] F. Isensee, P. F. Jaeger, S. A. Kohl, J. Petersen, and K. H. Maier-Hein, "nnu-net: a self-configuring method for deep learning-based biomedical image segmentation," *Nature Methods*, vol. 18, no. 2, pp. 203–211, 2021.
- [109] F. Isensee and K. H. Maier Hein, "An attempt at beating the 3d u-net," *arXiv*, 2019.
- [110] C. Li, Y. Tan, W. Chen, X. Luo, Y. Gao, X. Jia, and Z. Wang, "Attention unet++: A nested attention-aware u-net for liver ct image segmentation," in *IEEE International Conference on Image Processing (ICIP)*, 2020.
- [111] X. Li, L. Yu, H. Chen, C.-W. Fu, L. Xing, and P.-A. Heng, "Transformation-consistent self-ensembling model for semisupervised medical image segmentation," *IEEE Transactions on Neural Networks and Learning Systems*, vol. 32, no. 2, pp. 523–534, 2020.
- [112] S. Gul, M. S. Khan, A. Bibi, A. Khandakar, M. A. Ayari, and M. E. Chowdhury, "Deep learning techniques for liver and liver tumor segmentation: A review," *Computers in Biology and Medicine*, p. 105620, 2022.
- [113] D. T. Kushnure and S. N. Talbar, "Hfnet: High-level feature fusion and recalibration unet for automatic liver and tumor segmentation in ct images," *Computer Methods and Programs in Biomedicine*, vol. 213, p. 106501, 2022.
- [114] A. Paszke, S. Gross, F. Massa, A. Lerer, J. Bradbury, G. Chanan, T. Killeen, Z. Lin, N. Gimeshain, L. Antiga *et al.*, "Pytorch: An imperative style, high-performance deep learning library," in *Advances in Neural Information Processing Systems (NeurIPS)*, 2019.
- [115] D. Zhang, H. Zhang, J. Tang, X. Hua, and Q. Sun, "Causal intervention for weakly-supervised semantic segmentation," in *Advances in Neural Information Processing Systems (NeurIPS)*, 2020.
- [116] H. Li, G. Jiang, J. Zhang, R. Wang, Z. Wang, W. Zheng, and B. Menze, "Fully convolutional network ensembles for white matter hyperintensities segmentation in mr images," *NeuroImage*, vol. 183, no. 1, pp. 650–665, 2018.
- [117] F. Milletari, N. Navab, and S.-A. Ahmadi, "V-net: Fully convolutional neural networks for volumetric medical image segmentation," in *International Conference on 3D Vision (3DV)*, 2016.
- [118] T. Estienne, M. Vakalopoulou, E. Battistella, A. Carré, T. Henry, M. Lrousseau, C. Robert, N. Paragios, and E. Deutsch, "Deep learning based registration using spatial gradients and noisy segmentation labels," in *Medical Image Computing and Computer Assisted Intervention (MICCAI)*, 2020.
- [119] J. Deng, W. Dong, R. Socher, L. Li, K. Li, and L. Feifei, "Imagenet: A large-scale hierarchical image database," in *IEEE Conference on Computer Vision and Pattern Recognition (CVPR)*, 2009.
- [120] H.-C. Shin, N. A. Tenenholtz, J. K. Rogers, C. G. Schwarz, M. L. Senjem, J. L. Gunter, K. P. Andriole, and M. Michalski, "Medical image synthesis for data augmentation and anonymization using generative adversarial networks," in *Medical Image Computing and Computer Assisted Intervention (MICCAI)*, 2018.
- [121] D. P. Kingma and J. Ba, "Adam: A method for stochastic optimization," in *International Conference on Learning Representations (ICLR)*, 2015.
- [122] M. Drozdal, E. Vorontsov, G. Chartrand, S. Kadoury, and C. Pal, "The importance of skip connections in biomedical image segmentation," in *Deep Learning and Data Labeling for Medical Applications*, 2016, pp. 179–187.
- [123] G. Santini, N. Moreau, and M. Rubeaux, "Kidney tumor segmentation using an ensembling multi-stage deep learning approach. a contribution to the kits19 challenge," *arXiv*, 2019.
- [124] N. Ketkar, "Stochastic gradient descent," in *Deep Learning with Python*, 2017, pp. 113–132.
- [125] A. Qayyum, A. Lalande, and F. Meriaudeau, "Automatic segmentation of tumors and affected organs in the abdomen using a 3d hybrid model for computed tomography imaging," *Computers in Biology and Medicine*, vol. 127, no. 1, pp. 97–104, 2020.
- [126] X. Wang, R. Zhang, C. Shen, T. Kong, and L. Li, "Dense contrastive learning for self-supervised visual pre-training," in *IEEE Conference on Computer Vision and Pattern Recognition (CVPR)*, 2021.
- [127] T. Chen, S. Kornblith, M. Norouzi, and G. Hinton, "A simple framework for contrastive learning of visual representations," in *International Conference on Machine Learning (ICML)*, 2020.
- [128] K. He, H. Fan, Y. Wu, S. Xie, and R. Girshick, "Momentum contrast for unsupervised visual representation learning," in *IEEE Conference on Computer Vision and Pattern Recognition (CVPR)*, 2020.
- [129] Z. Zhou, V. Sodha, M. M. Rahman Siddiquee, R. Feng, N. Tajbakhsh, M. B. Gotway, and J. Liang, "Models genesis: Generic autodidactic models for 3d medical image analysis," in *Medical Image Computing and Computer Assisted Intervention (MICCAI)*, 2019.
- [130] I. Z. Yalniz, H. Jégou, K. Chen, M. Paluri, and D. Mahajan, "Billion-scale semi-supervised learning for image classification," *arXiv*, 2019.
- [131] D. Hendrycks, M. Mazeika, S. Kadavath, and D. Song, "Using self-supervised learning can improve model robustness and uncertainty," in *Advances in Neural Information Processing Systems (NeurIPS)*, 2019.
- [132] A. Kolesnikov, L. Beyer, X. Zhai, J. Puigcerver, J. Yung, S. Gelly, and N. Houlsby, "Big transfer (bit): General visual representation learning," in *European Conference on Computer Vision (ECCV)*, 2020.
- [133] J.-B. Grill, F. Strub, F. Altché, C. Tallec, P. Richemond, E. Buchatskaya, C. Doersch, B. Avila Pires, Z. Guo, M. Gheshlaghi Azar *et al.*, "Bootstrap your own latent—a new approach to self-supervised learning," in *Advances in Neural Information Processing Systems (NeurIPS)*, 2020, pp. 21 271–21 284.
- [134] L. Jing and Y. Tian, "Self-supervised visual feature learning with deep neural networks: A survey," *IEEE Transactions on Pattern Analysis and Machine Intelligence*, vol. 43, no. 11, pp. 4037–4058, 2020.
- [135] M. Chen, A. Radford, R. Child, J. Wu, H. Jun, D. Luan, and I. Sutskever, "Generative pretraining from pixels," in *International Conference on Machine Learning (ICML)*, 2020.
- [136] X. Chen and K. He, "Exploring simple siamese representation learning," in *IEEE Conference on Computer Vision and Pattern Recognition (CVPR)*, 2021.
- [137] A. Rajwade, A. Rangarajan, and A. Banerjee, "Image denoising using the higher order singular value decomposition," *IEEE Transactions on Pattern Analysis and Machine Intelligence*, vol. 35, no. 4, pp. 849–862, 2012.
- [138] A. Taleb, M. Kirchler, R. Monti, and C. Lippert, "Contig: Self-supervised multimodal contrastive learning for medical imaging with genetics," in *IEEE Conference on Computer Vision and Pattern Recognition (CVPR)*, 2022.
- [139] H. Zhao, Y. Li, N. He, K. Ma, L. Fang, H. Li, and Y. Zheng, "Anomaly detection for medical images using self-supervised and translation-consistent features," *IEEE Transactions on Medical Imaging*, vol. 40, no. 12, pp. 3641–3651, 2021.
- [140] F. Haghghi, M. R. H. Taher, Z. Zhou, M. B. Gotway, and J. Liang, "Transferable visual words: Exploiting the semantics of anatomical patterns for self-supervised learning," *IEEE Transactions on Medical Imaging*, vol. 40, no. 10, pp. 2857–2868, 2021.
- [141] X. Li, X. Hu, X. Qi, L. Yu, W. Zhao, P.-A. Heng, and L. Xing, "Rotation-oriented collaborative self-supervised learning for reti-

- nal disease diagnosis," *IEEE Transactions on Medical Imaging*, vol. 40, no. 9, pp. 2284–2294, 2021.
- [142] A. Kutikov and R. G. Uzzo, "The renal nephrometry score: a comprehensive standardized system for quantitating renal tumor size, location and depth," *The Journal of Urology*, vol. 182, no. 3, pp. 844–853, 2009.
- [143] S. Zheng, J. Lu, H. Zhao, X. Zhu, Z. Luo, Y. Wang, Y. Fu, J. Feng, T. Xiang, P. H. Torr *et al.*, "Rethinking semantic segmentation from a sequence-to-sequence perspective with transformers," in *IEEE Conference on Computer Vision and Pattern Recognition (CVPR)*, 2021.
- [144] H. Bao, L. Dong, F. Wei, W. Wang, N. Yang, X. Liu, Y. Wang, J. Gao, S. Piao, M. Zhou *et al.*, "Unilmv2: Pseudo-masked language models for unified language model pre-training," in *International Conference on Machine Learning (ICML)*, 2020.
- [145] M. N. Ahmed, S. M. Yamany, N. Mohamed, A. A. Farag, and T. Moriarty, "A modified fuzzy c-means algorithm for bias field estimation and segmentation of mri data," *IEEE Transactions on Medical Imaging*, vol. 21, no. 3, pp. 193–199, 2002.
- [146] Y. Zhang, M. Brady, and S. Smith, "Segmentation of brain mr images through a hidden markov random field model and the expectation-maximization algorithm," *IEEE Transactions on Medical Imaging*, vol. 20, no. 1, pp. 45–57, 2001.
- [147] Y. Lin, Z. Qu, H. Chen, Z. Gao, Y. Li, L. Xia, K. Ma, Y. Zheng, and K. T. Cheng, "Label propagation for annotation-efficient nuclei segmentation from pathology images," *arXiv*, 2022.
- [148] S. Kotsiantis, D. Kanellopoulos, P. Pintelas *et al.*, "Handling imbalanced datasets: A review," *GESTS International Transactions on Computer Science and Engineering*, vol. 30, no. 1, pp. 25–36, 2006.
- [149] S. M. Pizer, P. T. Fletcher, S. Joshi, A. Thall, J. Z. Chen, Y. Fridman, D. S. Fritsch, A. G. Gash, J. M. Glotzer, M. R. Jiroutek *et al.*, "Deformable m-reps for 3d medical image segmentation," *International Journal of Computer Vision*, vol. 55, no. 2, pp. 85–106, 2003.
- [150] H. Imai, S. Matzek, T. D. Le, Y. Negishi, and K. Kawachiya, "High resolution medical image segmentation using data-swapping method," in *Medical Image Computing and Computer Assisted Intervention (MICCAI)*, 2019.
- [151] M. H. Hesamian, W. Jia, X. He, and P. Kennedy, "Deep learning techniques for medical image segmentation: achievements and challenges," *Journal of Digital Imaging*, vol. 32, no. 4, pp. 582–596, 2019.
- [152] B. Mainak, K. Venkatanareshbabu, S. Luca, R. E. Damodar, C.-G. Elisa, M. R. Tato, N. Andrew *et al.*, "State-of-the-art review on deep learning in medical imaging," *Frontiers in Bioscience-Landmark*, vol. 24, no. 3, pp. 380–406, 2019.
- [153] B. Krawczyk, M. Koziarski, and M. Woźniak, "Radial-based over-sampling for multiclass imbalanced data classification," *IEEE Transactions on Neural Networks and Learning Systems*, vol. 31, no. 8, pp. 2818–2831, 2019.
- [154] N. V. Chawla, K. W. Bowyer, L. O. Hall, and W. P. Kegelmeyer, "Smote: synthetic minority over-sampling technique," *Journal of Artificial Intelligence Research*, vol. 16, no. 1, pp. 321–357, 2002.
- [155] H. Han, W.-Y. Wang, and B.-H. Mao, "Borderline-smote: a new over-sampling method in imbalanced data sets learning," in *International Conference on Intelligent Computing (ICIC)*, 2005, pp. 878–887.
- [156] H. He, Y. Bai, E. A. Garcia, and S. Li, "Adasyn: Adaptive synthetic sampling approach for imbalanced learning," in *IEEE International Joint Conference on Neural Networks (IJCNN)*, 2008.
- [157] W. Fithian and T. Hastie, "Local case-control sampling: Efficient subsampling in imbalanced data sets," *Annals of Statistics*, vol. 42, no. 5, p. 1693, 2014.
- [158] G. Lemaître, F. Nogueira, and C. K. Aridas, "Imbalanced-learn: A python toolbox to tackle the curse of imbalanced datasets in machine learning," *The Journal of Machine Learning Research*, vol. 18, no. 1, pp. 559–563, 2017.
- [159] M. Seppä, "High-quality two-stage resampling for 3-d volumes in medical imaging," *Medical Image Analysis*, vol. 11, no. 4, pp. 346–360, 2007.
- [160] C. Lartizien, J.-B. Aubin, and I. Buvat, "Comparison of bootstrap resampling methods for 3-d pet imaging," *IEEE Transactions on Medical Imaging*, vol. 29, no. 7, pp. 1442–1454, 2010.
- [161] Q. Zhu, B. Du, and P. Yan, "Boundary-weighted domain adaptive neural network for prostate mr image segmentation," *IEEE Transactions on Medical Imaging*, vol. 39, no. 3, pp. 753–763, 2019.
- [162] M. Shah, Y. Xiao, N. Subbanna, S. Francis, D. L. Arnold, D. L. Collins, and T. Arbel, "Evaluating intensity normalization on mris of human brain with multiple sclerosis," *Medical Image Analysis*, vol. 15, no. 2, pp. 267–282, 2011.
- [163] G. Collewet, M. Strzelecki, and F. Mariette, "Influence of mri acquisition protocols and image intensity normalization methods on texture classification," *Magnetic Resonance Imaging*, vol. 22, no. 1, pp. 81–91, 2004.
- [164] R. T. Shinohara, E. M. Sweeney, J. Goldsmith, N. Shiee, F. J. Mateen, P. A. Calabresi, S. Jarso, D. L. Pham, D. S. Reich, C. M. Crainiceanu *et al.*, "Statistical normalization techniques for magnetic resonance imaging," *NeuroImage*, vol. 6, no. 1, pp. 9–19, 2014.
- [165] D. Ulyanov, A. Vedaldi, and V. Lempitsky, "Instance normalization: The missing ingredient for fast stylization," *arXiv*, 2016.
- [166] C. Shorten and T. M. Khoshgoftaar, "A survey on image data augmentation for deep learning," *Journal of Big Data*, vol. 6, no. 1, pp. 1–48, 2019.
- [167] L. Taylor and G. Nitschke, "Improving deep learning with generic data augmentation," in *IEEE Symposium Series on Computational Intelligence (SSCI)*, 2018.
- [168] R. Hataya, J. Zdenek, K. Yoshizoe, and H. Nakayama, "Meta approach to data augmentation optimization," in *IEEE/CVF Winter Conference on Applications of Computer Vision (WACV)*, 2022.
- [169] G. Wang, W. Kang, Q. Wu, Z. Wang, and J. Gao, "Generative adversarial network (gan) based data augmentation for palm-print recognition," in *Digital Image Computing: Techniques and Applications (DICTA)*, 2018.
- [170] M. Xu, S. Yoon, A. Fuentes, and D. S. Park, "A comprehensive survey of image augmentation techniques for deep learning," *arXiv*, 2022.
- [171] A. Zhao, G. Balakrishnan, F. Durand, J. V. Guttag, and A. V. Dalca, "Data augmentation using learned transformations for one-shot medical image segmentation," in *IEEE Conference on Computer Vision and Pattern Recognition (CVPR)*, 2019.
- [172] J. Xu, M. Li, and Z. Zhu, "Automatic data augmentation for 3d medical image segmentation," in *Medical Image Computing and Computer Assisted Intervention (MICCAI)*, 2020.
- [173] P. Isola, J.-Y. Zhu, T. Zhou, and A. A. Efros, "Image-to-image translation with conditional adversarial networks," in *IEEE Conference on Computer Vision and Pattern Recognition (CVPR)*, 2017.
- [174] N. T. Tran, V. H. Tran, N. B. Nguyen, T. K. Nguyen, and N. M. Cheung, "On data augmentation for gan training," *IEEE Transactions on Image Processing*, vol. 30, no. 1, pp. 1882–1897, 2021.
- [175] S. Zhao, Z. Liu, J. Lin, J.-Y. Zhu, and S. Han, "Differentiable augmentation for data-efficient gan training," in *Advances in Neural Information Processing Systems (NeurIPS)*, 2020.
- [176] T. Karras, M. Aittala, J. Hellsten, S. Laine, J. Lehtinen, and T. Aila, "Training generative adversarial networks with limited data," in *Advances in Neural Information Processing Systems (NeurIPS)*, 2020.
- [177] X. Yi, E. Walia, and P. Babyn, "Generative adversarial network in medical imaging: A review," *Medical Image Analysis*, vol. 58, p. 101552, 2019.
- [178] D. Nie, R. Trullo, J. Lian, C. Petitjean, S. Ruan, Q. Wang, and D. Shen, "Medical image synthesis with context-aware generative adversarial networks," in *Medical Image Computing and Computer Assisted Intervention (MICCAI)*, 2017.
- [179] C.-Y. Lee, S. Xie, P. Gallagher, Z. Zhang, and Z. Tu, "Deeply-supervised nets," in *Artificial Intelligence and Statistics*, 2015, pp. 562–570.
- [180] Y. Zang, C. Huang, and C. C. Loy, "Fasa: Feature augmentation and sampling adaptation for long-tailed instance segmentation," in *IEEE/CVF International Conference on Computer Vision (ICCV)*, 2021.
- [181] W. R. Crum, O. Camara, and D. L. Hill, "Generalized overlap measures for evaluation and validation in medical image analysis," *IEEE Transactions on Medical Imaging*, vol. 25, no. 11, pp. 1451–1461, 2006.
- [182] T.-Y. Lin, P. Goyal, R. Girshick, K. He, and P. Dollár, "Focal loss for dense object detection," in *IEEE/CVF International Conference on Computer Vision (ICCV)*, 2017.
- [183] T. H. Phan and K. Yamamoto, "Resolving class imbalance in object detection with weighted cross entropy losses," *arXiv*, 2020.
- [184] A. Shrivastava, A. Gupta, and R. Girshick, "Training region-based object detectors with online hard example mining," in *IEEE Conference on Computer Vision and Pattern Recognition (CVPR)*, 2016.

- [185] K. He, X. Chen, S. Xie, Y. Li, P. Dollár, and R. Girshick, "Masked autoencoders are scalable vision learners," in *IEEE Conference on Computer Vision and Pattern Recognition (CVPR)*, 2022.
- [186] X. Chen, S. Xie, and K. He, "An empirical study of training self-supervised vision transformers," in *IEEE/CVF International Conference on Computer Vision (ICCV)*, 2021.
- [187] L. Wang, C. Y. Lee, Z. Tu, and S. Lazebnik, "Training deeper convolutional networks with deep supervision," *arXiv*, 2015.
- [188] D. Zhang, H. Zhang, J. Tang, X. Hua, and Q. Sun, "Self-regulation for semantic segmentation," in *IEEE/CVF International Conference on Computer Vision (ICCV)*, 2021.
- [189] M. Phuong and C. H. Lampert, "Distillation-based training for multi-exit architectures," in *IEEE/CVF International Conference on Computer Vision (ICCV)*, 2019.
- [190] D. Zhang, H. Zhang, J. Tang, M. Wang, X. Hua, and Q. Sun, "Feature pyramid transformer," in *European Conference on Computer Vision (ECCV)*, 2020.
- [191] C. Yu, J. Wang, C. Peng, C. Gao, G. Yu, and N. Sang, "Learning a discriminative feature network for semantic segmentation," in *IEEE Conference on Computer Vision and Pattern Recognition (CVPR)*, 2018.
- [192] H. Zhang, K. Dana, J. Shi, Z. Zhang, X. Wang, A. Tyagi, and A. Agrawal, "Context encoding for semantic segmentation," in *IEEE Conference on Computer Vision and Pattern Recognition (CVPR)*, 2018.
- [193] L. Chen, G. Papandreou, I. Kokkinos, K. Murphy, and A. L. Yuille, "DeepLab: Semantic image segmentation with deep convolutional nets, atrous convolution, and fully connected crfs," *IEEE Transactions on Pattern Analysis and Machine Intelligence*, vol. 40, no. 4, pp. 834–848, 2017.
- [194] C. Liu, L. Chen, F. Schroff, H. Adam, W. Hua, A. L. Yuille, and L. Fei Fei, "Auto-deeplab: Hierarchical neural architecture search for semantic image segmentation," in *IEEE Conference on Computer Vision and Pattern Recognition (CVPR)*, 2019.
- [195] L. A. Gatys, A. S. Ecker, and M. Bethge, "Image style transfer using convolutional neural networks," in *IEEE Conference on Computer Vision and Pattern Recognition (CVPR)*, 2016.
- [196] J. L. Ba, J. R. Kiros, and G. E. Hinton, "Layer normalization," *arXiv*, 2016.
- [197] K. Kamnitsas, W. Bai, E. Ferrante, S. McDonagh, M. Sinclair, N. Pawlowski, M. Rajchl, M. Lee, B. Kainz, D. Rueckert *et al.*, "Ensembles of multiple models and architectures for robust brain tumour segmentation," in *Workshop on Medical Image Computing and Computer Assisted Intervention (Workshop MICCAI)*, 2017.
- [198] D. Shanmugam, D. Blalock, G. Balakrishnan, and J. Guttag, "Better aggregation in test-time augmentation," in *IEEE/CVF International Conference on Computer Vision (ICCV)*, 2021.
- [199] N. Moshkov, B. Mathe, A. Kertesz-Farkas, R. Hollandi, and P. Horvath, "Test-time augmentation for deep learning-based cell segmentation on microscopy images," *Scientific Reports*, vol. 10, no. 1, pp. 1–7, 2020.
- [200] S. Luo, Y. Li, P. Gao, Y. Wang, and S. Serikawa, "Meta-seg: A survey of meta-learning for image segmentation," *Pattern Recognition*, p. 108586, 2022.
- [201] K. Han, Y. Wang, H. Chen, X. Chen, J. Guo, Z. Liu, Y. Tang, A. Xiao, C. Xu, Y. Xu *et al.*, "A survey on vision transformer," *IEEE Transactions on Pattern Analysis and Machine Intelligence*, 2022.
- [202] M. Havaei, A. Davy, D. Warde Farley, A. Biard, A. Courville, Y. Bengio, C. Pal, P.-M. Jodoin, and H. Larochelle, "Brain tumor segmentation with deep neural networks," *Medical Image Analysis*, vol. 35, pp. 18–31, 2017.
- [203] T. Chen and D. Metaxas, "A hybrid framework for 3d medical image segmentation," *Medical Image Analysis*, vol. 9, no. 6, pp. 547–565, 2005.
- [204] R. Dorent, A. Kujawa, M. Ivory, S. Bakas, N. Rieke, S. Joutard, B. Glocker, J. Cardoso, M. Modat, K. Batmanghelich *et al.*, "Crossmoda 2021 challenge: Benchmark of cross-modality domain adaptation techniques for vestibular schwannoma and cochlea segmentation," *arXiv*, 2022.
- [205] K. Saikumar, V. Rajesh, N. Ramya, S. H. Ahammad, and G. N. S. Kumar, "A deep learning process for spine and heart segmentation using pixel-based convolutional networks," *Journal of International Pharmaceutical Research*, vol. 46, no. 1, pp. 278–282, 2019.
- [206] F. Mahmood, R. Chen, and N. J. Durr, "Unsupervised reverse domain adaptation for synthetic medical images via adversarial training," *IEEE Transactions on Medical Imaging*, vol. 37, no. 12, pp. 2572–2581, 2018.
- [207] J. Sutherland, J. Belec, A. Sheikh, L. Chepelev, W. Althobaity, B. J. Chow, D. Mitsouras, A. Christensen, F. J. Rybicki, and D. J. La Russa, "Applying modern virtual and augmented reality technologies to medical images and models," *Journal of Digital Imaging*, vol. 32, no. 1, pp. 38–53, 2019.
- [208] S. J. Pan and Q. Yang, "A survey on transfer learning," *IEEE Transactions on Knowledge and Data Engineering*, vol. 22, no. 10, pp. 1345–1359, 2009.
- [209] K. Weiss, T. M. Khoshgoftaar, and D. Wang, "A survey of transfer learning," *Journal of Big data*, vol. 3, no. 1, pp. 1–40, 2016.
- [210] C. Tan, F. Sun, T. Kong, W. Zhang, C. Yang, and C. Liu, "A survey on deep transfer learning," in *International Conference on Artificial Neural Networks*, 2018.
- [211] T. Hospedales, A. Antoniou, P. Micaelli, and A. Storkey, "Meta-learning in neural networks: A survey," *arXiv*, 2020.
- [212] Z. Zhou, Z. Yang, S. Jiang, F. Zhang, and H. Yan, "Design and validation of a surgical navigation system for brachytherapy based on mixed reality," *Medical Physics*, vol. 46, no. 8, pp. 3709–3718, 2019.
- [213] Y. Na, L. Zhao, Y. Yang, and M. Ren, "Guided filter-based images fusion algorithm for ct and mri medical images," *IET Image Processing*, vol. 12, no. 1, pp. 138–148, 2018.
- [214] A. G. Roy, J. Ren, S. Azizi, A. Loh, V. Natarajan, B. Mustafa, N. Pawlowski, J. Freyberg, Y. Liu, Z. Beaver *et al.*, "Does your dermatology classifier know what it doesn't know? detecting the long-tail of unseen conditions," *Medical Image Analysis*, vol. 75, p. 102274, 2022.
- [215] P. Kumar and M. M. Srivastava, "Example mining for incremental learning in medical imaging," in *IEEE Symposium Series on Computational Intelligence (SSCI)*, 2018, pp. 48–51.
- [216] A. Kirillov, E. Mintun, N. Ravi, H. Mao, C. Rolland, L. Gustafson, T. Xiao, S. Whitehead, A. C. Berg, W.-Y. Lo *et al.*, "Segment anything," *arXiv*, 2023.
- [217] J. Ma and B. Wang, "Segment anything in medical images," *arXiv*, 2023.
- [218] T. Yu, R. Feng, R. Feng, J. Liu, X. Jin, W. Zeng, and Z. Chen, "Inpaint anything: Segment anything meets image inpainting," *arXiv*, 2023.
- [219] S. He, R. Bao, J. Li, P. E. Grant, and Y. Ou, "Accuracy of segment-anything model (sam) in medical image segmentation tasks," *arXiv*, 2023.
- [220] L. Tang, H. Xiao, and B. Li, "Can sam segment anything? when sam meets camouflaged object detection," *arXiv*, 2023.
- [221] R. Deng, C. Cui, Q. Liu, T. Yao, L. W. Remedios, S. Bao, B. A. Landman, L. E. Wheless, L. A. Coburn, K. T. Wilson *et al.*, "Segment anything model (sam) for digital pathology: Assess zero-shot segmentation on whole slide imaging," *arXiv*, 2023.
- [222] T. Zhou, Y. Zhang, Y. Zhou, Y. Wu, and C. Gong, "Can sam segment polyps?" *arXiv*, 2023.
- [223] C. Hu and X. Li, "When sam meets medical images: An investigation of segment anything model (sam) on multi-phase liver tumor segmentation," *arXiv*, 2023.
- [224] Y. Huang, X. Yang, L. Liu, H. Zhou, A. Chang, X. Zhou, R. Chen, J. Yu, J. Chen, C. Chen *et al.*, "Segment anything model for medical images?" *arXiv*, 2023.
- [225] J. Wu, R. Fu, H. Fang, Y. Liu, Z. Wang, Y. Xu, Y. Jin, and T. Arbel, "Medical sam adapter: Adapting segment anything model for medical image segmentation," *arXiv*, 2023.
- [226] D. Cheng, Z. Qin, Z. Jiang, S. Zhang, Q. Lao, and K. Li, "Sam on medical images: A comprehensive study on three prompt modes," *arXiv*, 2023.
- [227] K. Zhang and D. Liu, "Customized segment anything model for medical image segmentation," *arXiv*, 2023.
- [228] S. Wang, Z. Zhao, X. Ouyang, Q. Wang, and D. Shen, "Chatcad: Interactive computer-aided diagnosis on medical image using large language models," *arXiv*, 2023.
- [229] A. Radford, J. W. Kim, C. Hallacy, A. Ramesh, G. Goh, S. Agarwal, G. Sastry, A. Askell, P. Mishkin, J. Clark *et al.*, "Learning transferable visual models from natural language supervision," in *International Conference on Machine Learning (ICML)*, 2021.
- [230] K. Zhou, J. Yang, C. C. Loy, and Z. Liu, "Learning to prompt for vision-language models," *International Journal of Computer Vision*, vol. 130, no. 9, pp. 2337–2348, 2022.
- [231] L. Zhang and M. Agrawala, "Adding conditional control to text-to-image diffusion models," *arXiv*, 2023.